

EMC chaperone–Ca_v structure reveals an ion channel assembly intermediate

<https://doi.org/10.1038/s41586-023-06175-5>

Received: 3 October 2022

Accepted: 5 May 2023

Published online: 17 May 2023

 Check for updates

Zhou Chen¹, Abhishek Mondal¹, Fayal Abderemane-Ali^{1,8}, Seil Jang¹, Sangeeta Niranjan¹, José L. Montaño², Balyn W. Zaro^{1,2} & Daniel L. Minor Jr^{1,3,4,5,6,7}✉

Voltage-gated ion channels (VGICs) comprise multiple structural units, the assembly of which is required for function^{1,2}. Structural understanding of how VGIC subunits assemble and whether chaperone proteins are required is lacking. High-voltage-activated calcium channels (Ca_vs)^{3,4} are paradigmatic multisubunit VGICs whose function and trafficking are powerfully shaped by interactions between pore-forming Ca_v1 or Ca_v2 Ca_vα₁ (ref. 3), and the auxiliary Ca_vβ⁵ and Ca_vα₂δ subunits^{6,7}. Here we present cryo-electron microscopy structures of human brain and cardiac Ca_v1.2 bound with Ca_vβ₃ to a chaperone—the endoplasmic reticulum membrane protein complex (EMC)^{8,9}—and of the assembled Ca_v1.2–Ca_vβ₃–Ca_vα₂δ-1 channel. These structures provide a view of an EMC–client complex and define EMC sites—the transmembrane (TM) and cytoplasmic (Cyto) docks; interaction between these sites and the client channel causes partial extraction of a pore subunit and splay open the Ca_vα₂-interaction site. The structures identify the Ca_vα₂δ-binding site for gabapentinoid anti-pain and anti-anxiety drugs⁶, show that EMC and Ca_vα₂δ interactions with the channel are mutually exclusive, and indicate that EMC-to-Ca_vα₂δ hand-off involves a divalent ion-dependent step and Ca_v1.2 element ordering. Disruption of the EMC–Ca_v complex compromises Ca_v function, suggesting that the EMC functions as a channel holdase that facilitates channel assembly. Together, the structures reveal a Ca_v assembly intermediate and EMC client-binding sites that could have wide-ranging implications for the biogenesis of VGICs and other membrane proteins.

All VGIC superfamily members require assembly to make the functional channel^{1,2}. High-voltage-activated Ca_vs (Ca_v1 and Ca_v2)^{3,4} are ubiquitous in electrically excitable tissues such as the muscle, brain and heart and provide a paradigmatic example of a multisubunit VGIC comprising three key components—the pore-forming Ca_vα₁, cytoplasmic Ca_vβ⁵ and extracellular Ca_vα₂δ^{6,7} subunits. It has been known for more than 30 years that Ca_vβ and Ca_vα₂δ association with Ca_vα₁ profoundly shape Ca_v biophysical properties and plasma membrane expression^{5,10–13}. Ca_vα₂δ has a particularly important role in enhancing cell surface expression and is the target of widely used anti-nociceptive and anti-anxiety gabapentinoid drugs^{13–15} that bind to Ca_vα₂δ and impair surface expression^{14,16,17}.

The importance of subunit assembly for the biogenesis of properly functioning channels has been long appreciated^{2,18}. However, understanding of the steps involved or the extent to which chaperone proteins participate is lacking. The EMC is a nine-protein transmembrane assembly that is thought to aid the membrane insertion of tail-anchored proteins^{8,9,19,20} and transmembrane segments with mixed hydrophobic/hydrophilic character, such as those in ion channels^{21–23}, receptors^{24–26} and transporters^{22,24,27}. It may also function as holdase for partially assembled membrane proteins²⁶. Although recent structural studies

have outlined the EMC architecture and implicated various EMC client protein interaction sites based on mutational analysis^{26,28–30}, there are no structural examples of EMC–client-protein complexes to guide understanding of substrate protein binding.

Here we present cryo-electron microscopy (cryo-EM) structures of an approximately 0.6 MDa complex containing the human brain and heart Ca_v1.2 Ca_vα₁ subunit³, Ca_vβ₃ and human EMC, and the fully assembled Ca_v1.2–Ca_vβ₃–Ca_vα₂δ-1 channel, a Ca_vα₁–Ca_vβ combination^{3,5,31} that is present in human hearts³², at overall resolutions of 3.4 Å and 3.3 Å, respectively. This Ca_v is the target of drugs for cardiac and neurological diseases^{6,7,33} and is associated with many arrhythmia, autism and neuropsychiatric disease mutations^{3,4,34}. Our data provide a view of an EMC–client membrane protein complex and reveal EMC sites, the TM and Cyto docks, the interaction of which with conserved Ca_vα₁ and Ca_vβ elements results in a partial extraction of one of the channel pore domains (PDs) relative to its native position and splaying open of the Ca_vα₁ extracellular face where Ca_vα₂δ binds. Together, the structural data indicate that EMC and Ca_vα₂δ binding to the Ca_vα₁–Ca_vβ channel core is mutually exclusive and that EMC hand-off to Ca_vα₂δ involves ordering three extracellular sites that are splayed apart in the EMC complex. Notably, disrupting EMC–channel interactions by channel

¹Cardiovascular Research Institute, University of California, San Francisco, CA, USA. ²Department of Pharmaceutical Chemistry, University of California, San Francisco, CA, USA. ³Department of Biochemistry and Biophysics, University of California, San Francisco, CA, USA. ⁴California Institute for Quantitative Biomedical Research, University of California, San Francisco, CA, USA.

⁵Kavli Institute for Fundamental Neuroscience, University of California, San Francisco, CA, USA. ⁶Molecular Biophysics and Integrated Bio-imaging Division, Lawrence Berkeley National Laboratory, Berkeley, CA, USA. ⁷Department of Cellular and Molecular Pharmacology, University of California, San Francisco, CA, USA. ⁸Present address: Department of Physiology, David Geffen School of Medicine at UCLA, Los Angeles, CA, USA. [✉]e-mail: daniel.minor@ucsf.edu

mutations or EMC-subunit knockout diminishes channel activity, suggesting a role for the EMC as a Ca_v holdase. The $\text{Ca}_v1.2-\text{Ca}_v\beta_3-\text{Ca}_v\alpha_1\delta$ -binding site targeted by widely used gabapentinoid drugs^{35,36} for pain, fibromyalgia, posttherapeutic neuralgia and generalized anxiety disorder^{6,7}. Our data define a Ca_v assembly intermediate that establishes a framework for understanding Ca_v biogenesis, drug action^{3,6,37} and the consequences of Ca_v disease mutations affecting the brain, heart and endocrine systems^{4,34}. Owing to their conserved nature, the EMC-client interaction sites are likely to be exploited by many VGIC superfamily client proteins. Other membrane protein classes that have transmembrane segments of mixed hydrophobic and hydrophilic character⁹, such as transporters and G-protein-coupled receptors, may also engage these sites.

A stable ER chaperone-ion channel complex

Purification of $\text{Ca}_v1.2(\Delta C)$ —a recombinantly expressed human $\text{Ca}_v1.2$ construct bearing a C-terminal truncation distal to the Ile–Gln (IQ) domain with functional properties equivalent to full-length $\text{Ca}_v1.2$ (Supplementary Fig. 2) (186 kDa)—with rabbit $\text{Ca}_v\beta_3$ (54 kDa), yielded a sample displaying a good size-exclusion profile containing numerous unexpected bands (Extended Data Fig. 1a,b and Supplementary Fig. 1a,b). Mass spectrometry (MS) analysis showed that these bands comprise the 9 subunits of the approximately 300 kDa EMC^{8,9,19} that co-purified with $\text{Ca}_v1.2(\Delta C)-\text{Ca}_v\beta_3$ (Supplementary Table 1a). Cryo-EM images yielded two-dimensional class averages of a transmembrane complex with an unmistakable extramembrane EMC luminal domain crescent (Extended Data Fig. 1c,d). Co-expression of $\text{Ca}_v1.2(\Delta C)-\text{Ca}_v\beta_3$ with rabbit $\text{Ca}_v\alpha_2\delta-1$ (125 kDa) yielded a similarly behaved sample containing $\text{Ca}_v1.2(\Delta C)$, $\text{Ca}_v\beta_3$, $\text{Ca}_v\alpha_2\delta-1$ and all 9 EMC components (Extended Data Fig. 1e,f and Supplementary Fig. 1c,d) that also produced good cryo-EM images (Extended Data Fig. 1g,h). Single-particle analysis (Extended Data Fig. 1i) identified EMC– $\text{Ca}_v1.2(\Delta C)-\text{Ca}_v\beta_3$ complexes in both preparations and $\text{Ca}_v1.2(\Delta C)-\text{Ca}_v\beta_3-\text{Ca}_v\alpha_2\delta-1$ in the sample with $\text{Ca}_v1.2(\Delta C)$, $\text{Ca}_v\beta_3$ and $\text{Ca}_v\alpha_2\delta-1$. The resultant EMC– $\text{Ca}_v1.2(\Delta C)-\text{Ca}_v\beta_3$ and EMC– $\text{Ca}_v1.2(\Delta C)-\text{Ca}_v\beta_3-\text{Ca}_v\alpha_2\delta-1$ maps had overall resolutions of 3.4 Å and 3.3 Å (Supplementary Fig. 3a,b) and local resolutions of 2.4 Å and 2.0 Å, respectively (Extended Data Fig. 2, Extended Data Table 1 and Supplementary Figs. 3–6), and clearly defined the subunits of the eleven-protein EMC– $\text{Ca}_v1.2(\Delta C)-\text{Ca}_v\beta_3$ complex (Extended Data Fig. 2a,b) and the tripartite $\text{Ca}_v1.2(\Delta C)-\text{Ca}_v\beta_3-\text{Ca}_v\alpha_2\delta-1$ channel assembly (Extended Data Fig. 2c,d).

Structure of the EMC– $\text{Ca}_v1.2(\Delta C)-\text{Ca}_v\beta_3$ complex

The EMC– $\text{Ca}_v1.2(\Delta C)-\text{Ca}_v\beta_3$ complex is an approximately 0.6 MDa assembly with dimensions of about 220 Å normal to the membrane plane and around 100 Å × 130 Å parallel to the membrane plane (Fig. 1a). There are extensive $\text{Ca}_v1.2$ and $\text{Ca}_v\beta_3$ interactions with the EMC (Fig. 1a) comprising two binding sites—the TM dock and Cyto dock. These two sites are around 90° apart from each other with respect to the EMC core and engage transmembrane and cytoplasmic elements of the $\text{Ca}_v1.2-\text{Ca}_v\beta_3$ channel complex, respectively (Fig. 1b,c and Supplementary Video 1).

The TM dock comprises a large interface (1,051 Å²) in which the single EMC1 transmembrane helix (EMC1 TM) binds to the groove between the IS1 and IS2 transmembrane helices of the first $\text{Ca}_v1.2$ voltage-sensor domain (VSD1) (Fig. 1b–d and Extended Data Fig. 3a,b) using van der Waals interactions along the entire interface (Extended Data Fig. 3a,b) that are framed by luminal and inner bilayer leaflet hydrophilic interaction sites (Fig. 1d). The luminal site involves a salt bridge between Asp961 of EMC1, a conserved residue implicated in interaction with client proteins with a hydrophilic character³⁰, and Arg161 of $\text{Ca}_v1.2$ VSD1, a residue that is found in all Ca_v1 s except for $\text{Ca}_v1.4$, and $\text{Ca}_v2.3$ (Extended Data Fig. 3c). The inner leaflet site entails

a cation–π interaction³⁸ between the EMC1 Arg981 guanidinium and the $\text{Ca}_v1.2$ IS1 Trp123 indole that, with IS1 Ile120, frames a conserved hydrophobic pocket—the cation–π pocket (Extended Data Fig. 3a,b). Preservation of these two hydrophilic interaction sites and the IS1–IS2 surface among Ca_v1 s and Ca_v2 s (Extended Data Fig. 3c) suggests that other Ca_v VSDs interact similarly with the EMC. Furthermore, the interfacial EMC1 helix (brace²⁶ or crossbar²⁸ helix, hereafter brace/crossbar helix) extends its C-terminal end to contact the VSD I–PD II interface (Fig. 1c,e).

The Cyto dock (around 1,500 Å²) is composed of interactions between the EMC cytoplasmic cap (EMC2, EMC3, EMC4, EMC5 and EMC8) and $\text{Ca}_v\beta_3$ (Fig. 1f) and involves two sites. In the larger site (the EMC8 site, 962 Å²), two $\text{Ca}_v\beta$ nucleotide kinase domain loops (the β7–α4 loop, Thr218–Ala243; and β8–β9 loop, Pro277–Lys282) bind at a site of which the centre is formed by the last EMC8 helix (Fig. 1f). This interaction involves a hydrogen bond and salt bridge network of seven conserved $\text{Ca}_v\beta$ residues (Fig. 1f and Extended Data Fig. 3d–f) and includes a region, Lys225–Ser245, that is disordered in the isolated $\text{Ca}_v\beta_3$ (ref. 39) (Extended Data Fig. 3g) but that becomes ordered after EMC8 binding, suggesting that its conservation is linked to its EMC-binding role. In the smaller site (the EMC2 site, 550 Å²), $\text{Ca}_v\beta$ contacts the EMC2 N-terminal region through van der Waals interactions (Fig. 1f and Extended Data Fig. 3f–h). This site involves $\text{Ca}_v\beta$ α5 and α6 helices that are part of the α-binding pocket where $\text{Ca}_v\beta$ s make high-affinity interactions to the $\text{Ca}_v\alpha_1\alpha$ -interaction domain (AID)^{40,41}. The shared $\text{Ca}_v\beta$ architecture^{40,41} and contact residue conservation indicate that all $\text{Ca}_v\beta$ isoforms should bind to the Cyto dock.

Although the TM dock site is consistent with functional data implicating EMC1 Asp961 in client protein interaction³⁰, the EMC1 TM– $\text{Ca}_v1.2$ VSD I interface is on the opposite side of the EMC3-, EMC5- and EMC6-gated transmembrane cavity proposed to act in membrane protein insertion^{26,29,42}. The side of the channel facing the brace/crossbar helix surrounds the inner, hydrophobic, lipid-filled cavity formed by EMC1, EMC3, EMC5 and EMC6 (refs. 26,28,29,42) but, apart from the EMC1 brace/crossbar helix interactions, there are no other cavity elements interactions. The Cyto dock site is on the opposite side of the membrane from the EMC1, EMC7 and EMC10 luminal domain elements that were previously suggested to have a holdase function²⁶. Furthermore, the EMC2 and EMC8 sites are not near any cytoplasmic cap elements proposed for client interactions²⁸. Thus, the structure presents an EMC-client binding mode. Importantly, $\text{Ca}_v1.2-\text{Ca}_v\beta_3$ interactions with the TM dock and Cyto dock involve highly conserved channel subunit elements (Extended Data Fig. 3c,f), suggesting that Ca_v s comprising various combinations of $\text{Ca}_v\alpha_1$ and $\text{Ca}_v\beta$ ^{3,5} can also make the observed EMC-client interactions.

A $\text{Ca}_v\alpha_2\delta$ drug-binding site and a blocking lipid

The structure of $\text{Ca}_v1.2(\Delta C)-\text{Ca}_v\beta_3-\text{Ca}_v\alpha_2\delta-1$ (Fig. 2a, Extended Data Fig. 2c,d and Supplementary Fig. 6) reveals a tripartite channel assembly (around 370 kDa) with an overall structure similar to other Ca_v1 and Ca_v2 complexes (root mean squared deviation (r.m.s.d.)_{Ca} = 1.95 Å, 1.71 Å and 2.37 Å for $\text{Ca}_v\alpha_1$ from $\text{Ca}_v1.1$, $\text{Ca}_v1.3$ and $\text{Ca}_v2.2$, respectively)^{43–45} and $\text{Ca}_v\alpha_1$ subunit structure similar to single component Ca_v3 s (r.m.s.d._{Ca} = 2.28 Å for $\text{Ca}_v\alpha_1$ from $\text{Ca}_v3.1$)⁴⁶ (Supplementary Fig. 7a–d). As with most Ca_v structures^{43–45}, the $\text{Ca}_v1.2$ pore inner gate is closed and all four voltage sensors are in the ‘up’ conformation, consistent with a depolarized state and similar to $\text{Ca}_v1.3$ (ref. 44) (Extended Data Fig. 4a–d and Supplementary Fig. 7e–h). Moreover, similar to other Ca_v s^{43–45}, the proteolytic cleavage site dividing $\text{Ca}_v\alpha_2$ from $\text{Ca}_v\delta$ is disordered. Two notable features stand out. The first is a free leucine, a $\text{Ca}_v\alpha_2\delta$ ligand^{47,48} and gabapentin competitor^{6,37}, in the $\text{Ca}_v\alpha_2\delta-1$ Cache1 domain⁴⁹ hydrophobic pocket of the gabapentinoid drug-binding site^{6,7,35,36,50}. The high local resolution of this site (2.0–2.4 Å) shows the free leucine, obtained endogenously during expression, bound to a pocket lined

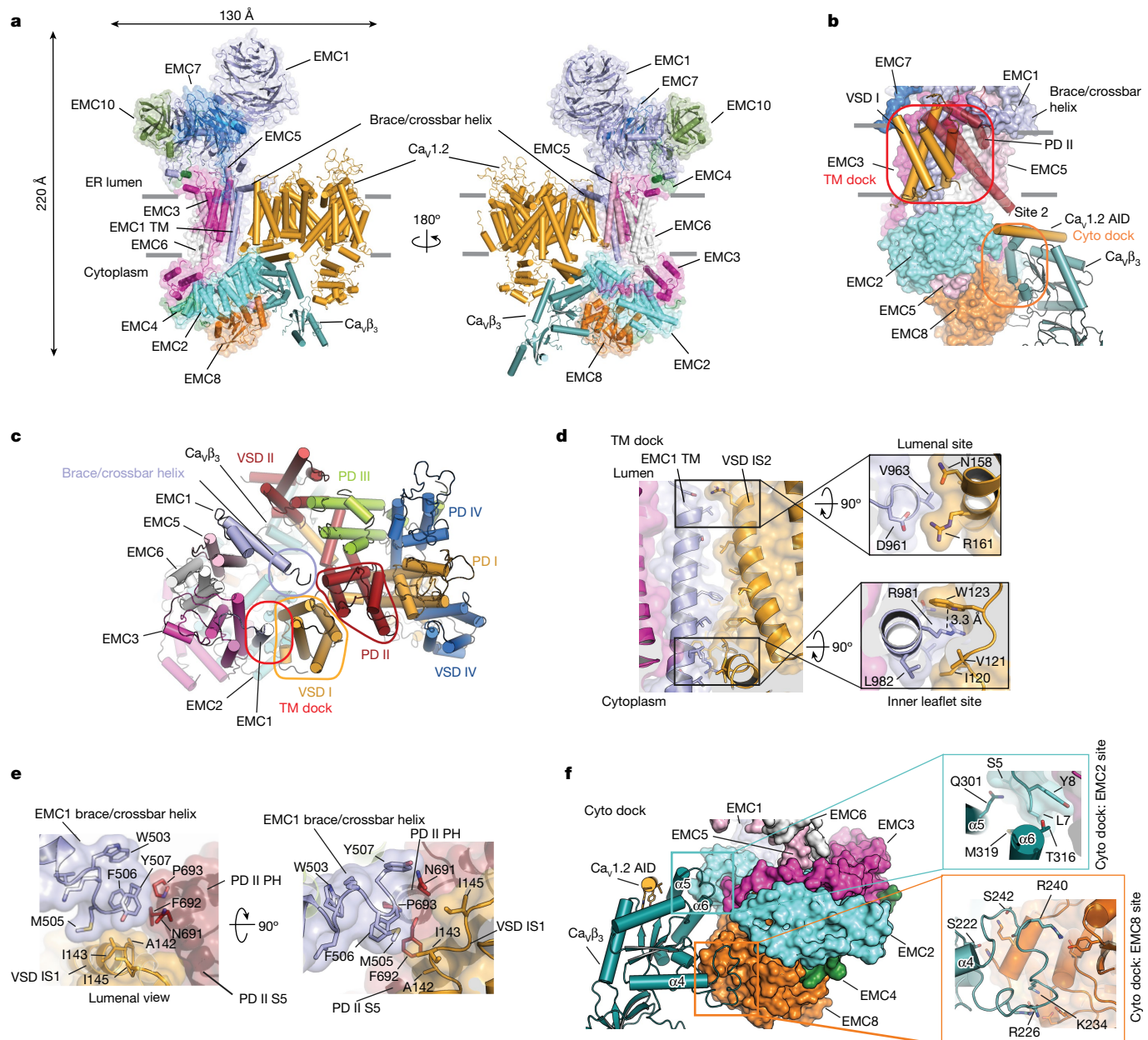


Fig. 1 | The structure of the EMC–Ca_v1.2(ΔC)–Ca_vβ₃ complex. **a**, Cartoon structure side views of the EMC–Ca_v1.2(ΔC)–Ca_vβ₃ complex. EMC1, EMC2, EMC3, EMC4, EMC5, EMC6, EMC7, EMC8, EMC10, Ca_v1.2 and Ca_vβ₃ are shown. EMC subunits are shown with semi-transparent surfaces. The arrows indicate dimensions. **b**, The location of the TM dock and Cyto dock EMC client-binding sites. Ca_v1.2 components interacting with the EMC are shown as cylinders. The AID helix is also shown. The grey bars in **a** and **b** denote the membrane. **c**, Luminal view of the EMC–Ca_v1.2(ΔC)–Ca_vβ₃ complex transmembrane elements. EMC components are shown as cylinders. Ca_v1.2(ΔC) domains are coloured as domain I (yellow orange), domain II (dark red), domain III (lime) and

domain IV (deep blue). VSD and PD elements are labelled. The red oval in **b** and **c** shows the TM dock site. The pale purple circle shows the site of interaction of the EMC1 brace/crossbar helix with Ca_v1.2 VSD I and PD II (outlined). **d**, Side view of the TM dock–VSD I interaction. Insets: details of interactions in the luminal site and inner leaflet side. EMC1 and Ca_v1.2 VSD I are shown. **e**, Details of the EMC1 brace/crossbar helix with Ca_v1.2 VSD I and PD II. **f**, Details of the Cyto dock. Ca_vβ₃ and AID helix are shown as cylinders. EMC2, EMC3, EMC4, EMC5, EMC6 and EMC8 are shown as surfaces. Insets: details of the EMC2 and EMC8 sites.

by Trp207, Val209, Tyr219, Trp225, Tyr238, Arg243, Trp245, Tyr452, Asp454, Ala455, Leu456 and Asp493 (Fig. 2b, Extended Data Fig. 4e and Supplementary Fig. 6j) in agreement with the prediction of this pocket as the leucine-binding site⁵⁰. The L-Leu backbone elements, shared with gabapentinoïds³⁷, are coordinated through salt bridge and hydrogen bond interactions to its carboxylate by Tyr238, Arg243 and Trp245 and a salt bridge between the amino nitrogen and Asp493 (Fig. 2b and Extended Data Fig. 4e), and are consistent with the importance of Arg243 (Arg217 in some numberings)^{14,51} and Asp493 (ref. 50) for gabapentinoïd drug-binding and action in pain modulation¹⁴. These data, together with studies establishing binding competition between leucine and gabapentin^{6,37} and recent Ca_vα₂δ structures with gabapentin³⁵ and mirogabalin³⁶ identify this Cache1 domain as the gabapentinoïd drug-binding site.

The second notable feature is a lipid, phosphatidylethanolamine (PE) (1-heptadecanoyl-2-dodecanoyl-glycero-3-phosphoethanolamine (17:0/12:0)), that fills a hydrophobic gap between PD I and PD II (Fig. 2c and Supplementary Fig. 6c). The phosphatidylethanolamine

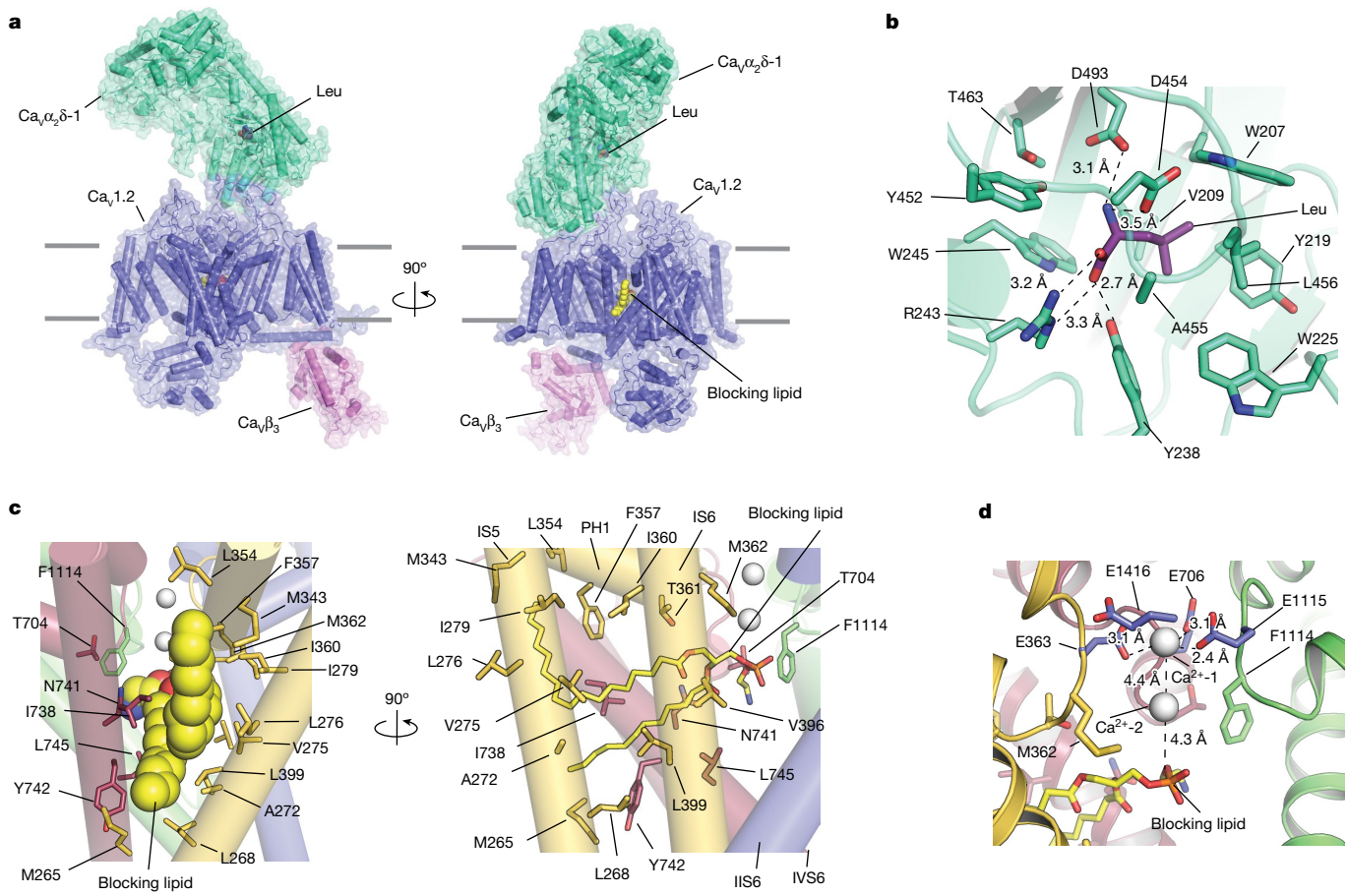


Fig. 2 | The structure of the $\text{Ca}_v1.2(\Delta\text{C})-\text{Ca}_v\beta_3-\text{Ca}_v\alpha_6\delta-1$ channel complex. **a**, Side views of $\text{Ca}_v1.2(\Delta\text{C})-\text{Ca}_v\beta_3-\text{Ca}_v\alpha_6\delta-1$. Leucine and blocking lipid are shown as space filling. The grey bars denote the membrane. **b**, Details of the $\text{Ca}_v\alpha_6\delta-1$ Cache1 ligand-binding site. Leucine (purple) and contacting side chains from $\text{Ca}_v\alpha_6\delta 1$ (green cyan) are shown as sticks. **c**, Details of the blocking lipid-binding site. $\text{Ca}_v1.2$ PDs are shown as cylinders and coloured as follows:

PD I (yellow orange), PD II (dark red), PD III (lime) and PD IV (deep blue). Lipid-contact residues are shown as sticks. Blocking lipid is shown as space filling (left) and sticks (right). **d**, Interaction between the blocking lipid and SF ions. Hallmark SF calcium-binding residues are shown as sticks (purple). SF calcium ions are indicated.

hydrophilic headgroup resides in the central pore below the selectivity filter (SF), where it coordinates the inner of two SF calcium ions (Fig. 2c,d, Extended Data Fig. 4f and Supplementary Fig. 6c) that match those in $\text{Ca}_v1.1$ (refs. 43,52), $\text{Ca}_v3.1$ (ref. 46) and $\text{Ca}_v3.3$ (ref. 53). Similarly, intrusive lipids between $\text{Ca}_v1.1$ PD I and PD II^{52,54} and $\text{Ca}_v3.3$ PD III and PD IV⁵³ emerge into the central cavity in the presence of pore-blocking drugs. $\text{Ca}_v1.1$ (refs. 43,52,54) and $\text{Ca}_v3.1$ (ref. 46) structures identified lipid tails in the equivalent PDI–PD II interface but did not resolve the headgroup. Owing to its interference of the ion path in the absence of drugs, we denote the $\text{Ca}_v1.2$ phosphatidylethanolamine as the blocking lipid. The presence of the blocking lipid polar headgroup in the central cavity in direct coordination with an SF Ca^{2+} ion shows that this lipid does not require a third-party molecule in the pore, such as a drug^{52–54}, and raises questions about whether and how this element contributes to channel gating and pharmacology.

Binding requires multiple rigid-body changes

Observation of the same channel complex $\text{Ca}_v1.2(\Delta C)-\text{Ca}_v\beta_3$ in two states—the EMC-bound form versus the fully assembled channel—reveals multiple conformational changes that substantially remodel the Ca_v structure after EMC binding (Fig. 3a and Supplementary Videos 2 and 3). The $\text{Ca}_v1.2$ VSD I, VSD II and VSD IV S4 segments correspond to a voltage sensor ‘up’ state in which gating charge residues (VSD I: K1,

R2, R3 and R4; VSD II: R2, R3 and R4; and VSD IV: R2, R3 and R4) are on the extracellular/luminal side of the aromatic position that defines the charge transfer centre⁵⁵ (Supplementary Fig. 8a–c). Although VSD I and VSD II are similar to those in Ca_v1.2(ΔC)–Ca_vβ₃–Ca_vα₂δ₁ (Supplementary Fig. 8d,e) (r.m.s.d._{Ca} = 0.69 Å and 2.25 Å for VSD I and VSD II, respectively) both undergo substantial rigid body displacements after EMC binding (Fig. 3a and Supplementary Videos 2–5). VSD III and VSD IV (Supplementary Fig. 8f) (r.m.s.d._{Ca} = 2.35 Å for VSD IV) undergo various degrees of rearrangement (Fig. 3a and Supplementary Videos 2, 3 and 6), the most notable of which is the unfolding of the majority of VSD III (Fig. 3a).

Viewed from the IS1-IS2 groove, VSD I rotates about 20° around an axis parallel with the membrane plane towards the channel periphery to engage the EMC1 TM helix (Supplementary Videos 2 and 4) and rotates approximately 10° within the membrane plane towards VSD IV (Fig. 3a and Extended Data Fig. 5a). VSD II tips away from the central pore by about 15° resulting in a displacement of the extracellular/lumenal ends of its helices by around 6 Å (Fig. 3a, Extended Data Fig. 5a and Supplementary Video 5). With the exception of the S4 C-terminal end, VSD III is largely disordered in the EMC–Ca_v complex. This lack of structure is apparent in the detergent micelle shape surrounding the channel (Extended Data Fig. 2b and d). VSD IV undergoes a complex set of changes in which S3 and S4 are repositioned relative to the S1–S2 pair, and rotates about 10° within the plane of the membrane towards

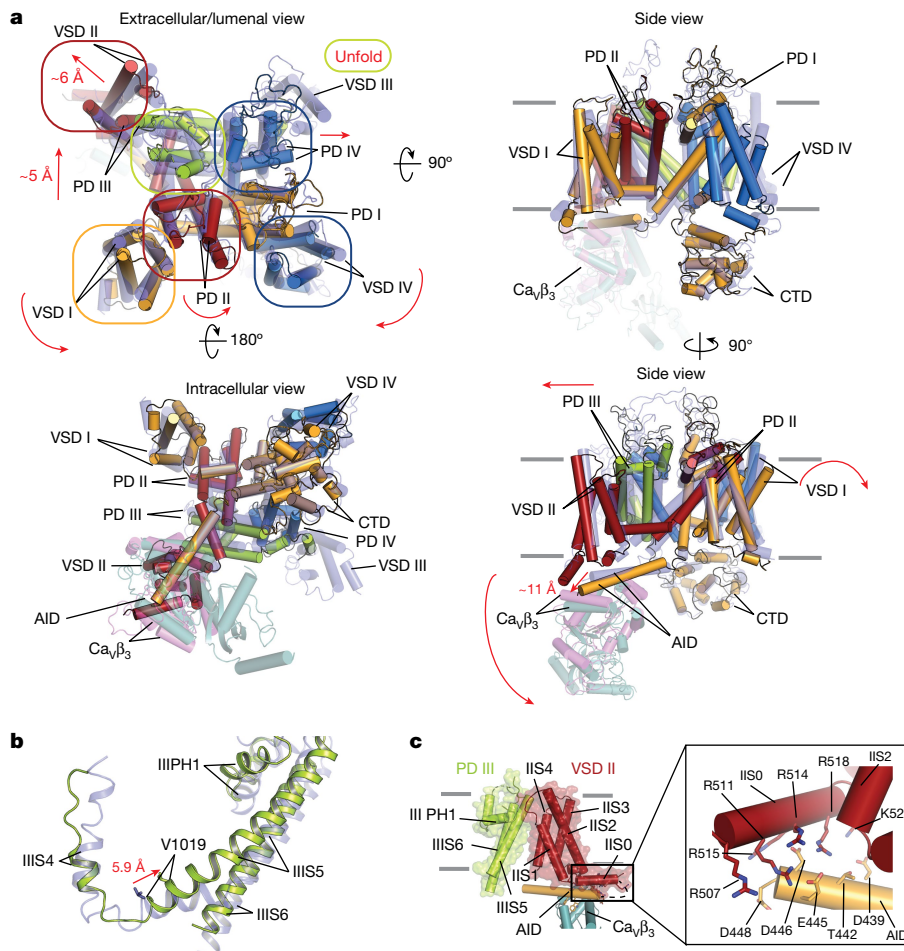


Fig. 3 | EMC interactions remodel Ca_v structure and extract PD III.

a, Superposition of $\text{Ca}_v1.2-\text{Ca}_v\beta_3$ from the EMC and $\text{Ca}_v1.2(\Delta C)-\text{Ca}_v\beta_3-\text{Ca}_v\alpha_2\delta-1$ complexes. $\text{Ca}_v1.2$ elements from the EMC complex are coloured as follows: VSD I/PD I (yellow orange), VSD II/PD II (dark red), VSD III/PD III (lime) and VSD IV/PD IV (deep blue). $\text{Ca}_v1.2$ (purple) and $\text{Ca}_v\beta_3$ (magenta) from $\text{Ca}_v1.2(\Delta C)-\text{Ca}_v\beta_3-\text{Ca}_v\alpha_2\delta-1$ are semi-transparent. The red arrows indicate conformational changes between $\text{Ca}_v1.2(\Delta C)-\text{Ca}_v\beta_3-\text{Ca}_v\alpha_2\delta-1$

and EMC- $\text{Ca}_v1.2(\Delta C)-\text{Ca}_v\beta_3$. Coloured ovals highlight key domains reshaped by the EMC. **b**, Superposition of the S4 and S4-S5 linker-PD III elements from the EMC- $\text{Ca}_v1.2(\Delta C)-\text{Ca}_v\beta_3$ complex (lime) and $\text{Ca}_v1.2(\Delta C)-\text{Ca}_v\beta_3-\text{Ca}_v\alpha_2\delta-1$ (purple). The $\text{C}\alpha-\text{C}\alpha$ distance for Val1019 is indicated. **c**, Interactions within the $\text{Ca}_v\beta$ -AID-VSD II-PD III subcomplex in EMC- $\text{Ca}_v1.2(\Delta C)-\text{Ca}_v\beta_3$. The grey bars in **a** and **c** denote the membrane.

VSD I (Fig. 3a, Extended Data Fig. 5a and Supplementary Videos 2 and 6). Thus, the relative conformations of all four VSDs change as a consequence of EMC binding.

Three out of the four PDs in the EMC complex are also altered relative to $\text{Ca}_v1.2(\Delta C)-\text{Ca}_v\beta_3-\text{Ca}_v\alpha_2\delta-1$. The most marked change is PD III. This PD is partially extracted from the central pore and displaced towards the channel periphery by around 5 \AA (Fig. 3a, Extended Data Fig. 5b and Supplementary Videos 2 and 3). Notably, despite some internal shifts (r.m.s.d. $_{\text{C}\alpha} = 3.269 \text{ \AA}$), the PD III tertiary fold comprising the IIIS5, PH1 and IIIS6 helices retains a near-native conformation (Extended Data Fig. 5b and Supplementary Video 7), consistent with the recent demonstration that the VGIC PD tertiary structure is independent of the quaternary structure⁵⁶. PD III PH2 is displaced by around 15° and the large extracellular loops connected to it are disordered. The other PD tertiary structures are largely unaltered (r.m.s.d. $_{\text{C}\alpha} = 0.91 \text{ \AA}, 0.46 \text{ \AA}$ and 1.17 \AA for PD I, PD II and PD IV, respectively) but, as a consequence of PD III extraction, PD II and PD IV undergo rigid-body changes, tipping towards and away from the pore central axis, respectively (Supplementary Videos 2, 3, 8 and 9). Extraction of PD III pulls the domain III S4-S5 linker along the lateral side of the channel by one helical turn, approximately 6 \AA (Fig. 3b and Supplementary Video 3), disturbing VSD III and leading to its unfolding (Fig. 3a and Extended Data Fig. 5a).

Binding to EMC reshapes the channel pore

Comparison of $\text{Ca}_v\beta_3$ in the EMC and $\text{Ca}_v1.2(\Delta C)-\text{Ca}_v\beta_3-\text{Ca}_v\alpha_2\delta-1$ complexes reveals conformational changes associated with EMC intracellular cap binding that explain the mechanism of PD III extraction from the central pore. To bind to the Cyto dock, $\text{Ca}_v\beta_3$ rotates about 5° away from its $\text{Ca}_v1.2(\Delta C)-\text{Ca}_v\beta_3-\text{Ca}_v\alpha_2\delta-1$ position close to the membrane (Fig. 3a and Extended Data Fig. 5c) and transmits this conformational change to the channel through the $\text{Ca}_v1.2$ AID helix. This element remains bound to $\text{Ca}_v\beta_3$ and tilts about 15° away from the membrane plane, displacing its C-terminal end by approximately 11 \AA relative to its $\text{Ca}_v1.2(\Delta C)-\text{Ca}_v\beta_3-\text{Ca}_v\alpha_2\delta-1$ position (Fig. 3a and Extended Data Fig. 5c) and enabling four AID acidic residues (Asp439, Glu445, Asp446 and Asp448) opposite to its $\text{Ca}_v\beta_3$ interface to interact with five VSD II IISO helix basic residues (Arg507, Arg511, Arg514, Arg515 and Arg518) (Fig. 3c). This interaction is absent in $\text{Ca}_v1.2(\Delta C)-\text{Ca}_v\beta_3-\text{Ca}_v\alpha_2\delta-1$ (Extended Data Fig. 5d) and occurs because IISO becomes more helical in the EMC complex (Extended Data Fig. 5d). These electrostatic interactions provide a link that pulls VSD II away from the channel central axis as a consequence of AID tilt (Fig. 3a). As VSD II IIS1 and IIS4 extracellular/luminal ends make numerous contacts with PD III IIIS5 and PH1 (Fig. 3c and Extended Data Fig. 5e) that are maintained

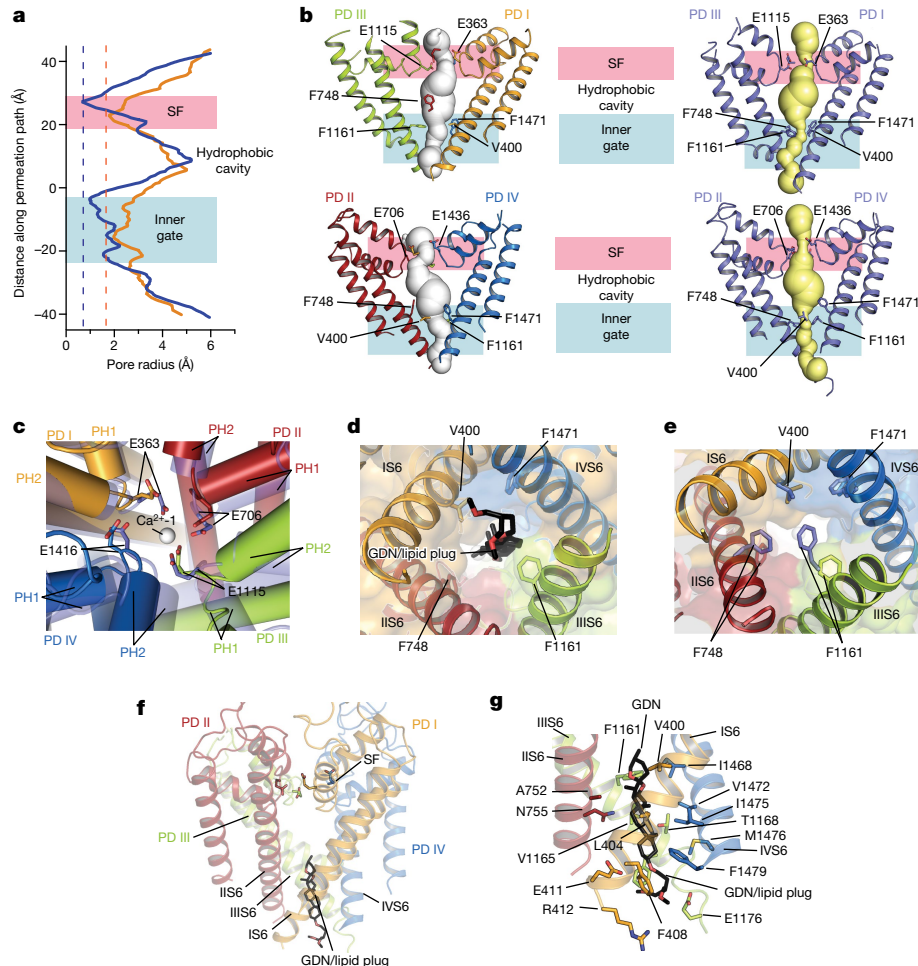


Fig. 4 | EMC association causes $\text{Ca}_\nu 1.2$ pore structural changes. **a**, $\text{Ca}_\nu 1.2$ pore profile comparison for EMC– $\text{Ca}_\nu 1.2(\Delta C)$ – $\text{Ca}_\nu \beta_3$ (orange) and $\text{Ca}_\nu 1.2(\Delta C)$ – $\text{Ca}_\nu \beta_3$ – $\text{Ca}_\nu \alpha_2\delta 1$ (blue), calculated using HOLE⁷². EMC: SF = 1.78 Å, inner gate = 1.98 Å; $\text{Ca}_\nu 1.2$: SF = 0.65 Å, inner gate = 0.98 Å. **b**, Side views of EMC– $\text{Ca}_\nu 1.2(\Delta C)$ – $\text{Ca}_\nu \beta_3$ (left) and $\text{Ca}_\nu 1.2(\Delta C)$ – $\text{Ca}_\nu \beta_3$ – $\text{Ca}_\nu \alpha_2\delta 1$ (right) pore profiles calculated using MOLE⁷³. The SF, central cavity and hydrophobic gate regions are indicated. SF and intracellular gate residues are shown. **c**, Comparison of the $\text{Ca}_\nu 1.2$ SF filter regions in the EMC– $\text{Ca}_\nu 1.2(\Delta C)$ – $\text{Ca}_\nu \beta_3$ pore (PD I, PD II, PD III and PD IV) and

$\text{Ca}_\nu 1.2(\Delta C)$ – $\text{Ca}_\nu \beta_3$ – $\text{Ca}_\nu \alpha_2\delta 1$ (semi-transparent, purple). Ca^{2+} -1 from $\text{Ca}_\nu 1.2(\Delta C)$ – $\text{Ca}_\nu \beta_3$ – $\text{Ca}_\nu \alpha_2\delta 1$ is shown as a white sphere. **d,e**, View of the $\text{Ca}_\nu 1.2$ intracellular gate from EMC– $\text{Ca}_\nu 1.2(\Delta C)$ – $\text{Ca}_\nu \beta_3$ (**d**) and $\text{Ca}_\nu 1.2(\Delta C)$ – $\text{Ca}_\nu \beta_3$ – $\text{Ca}_\nu \alpha_2\delta 1$ (**e**). GDN is shown as sticks. PDs are coloured as follows: PD I (yellow orange), PD II (dark red), PD III (lime) and PD IV (deep blue). **f,g**, Side views of the EMC– $\text{Ca}_\nu 1.2(\Delta C)$ – $\text{Ca}_\nu \beta_3$ pore showing global (**f**) and detailed (**g**) views. SF glutamates in **e** and GDN-contacting residues in **f,g** shown as sticks. PD elements are labelled.

in both structures, VSD II movement pulls PD III away from the central pore. The PD III–VSD II–AID– $\text{Ca}_\nu \beta_3$ assembly therefore acts as single unit of which the positions are transformed by the EMC– $\text{Ca}_\nu \beta_3$ interaction to effect the partial extraction of PD III from the central pore assembly, displacement of helical S4–S5 linker between IIIS4 and IIIS5 by about 6 Å (Supplementary Videos 2 and 3) and VSD III destabilization (Fig. 3a,b).

PD III extraction substantially reshapes the ion-conduction pathway. The overall pore diameter increases due to changes at its two narrowest points—the SF and inner gate (Fig. 4a,b and Extended Data Fig. 6)—that widen by about 1.1 Å and 1.0 Å, respectively, to create a water-filled pore that bridges the channel cytoplasmic and luminal sides (Fig. 4b and Extended Data Fig. 6). SF expansion affects the SF glutamate ring outer ion coordination site (Glu363, Glu706, Glu1115 and Glu1416) (Fig. 4c), while inner gate widening creates a pathway in which we find density for a bound glycol-diosgenin (GDN) (Fig. 4d–g, Extended Data Fig. 6 and Supplementary Fig. 4f). This GDN sits at a position similar to that seen in a drug-bound $\text{Ca}_\nu 1.1$ –verapamil complex with a widened inner gate⁵² and may mimic a natural lipid similar to GDN, such as cholesterol, that would serve as a plug to prevent ion leak through the EMC-bound pore. We therefore denote this as the lipid plug (Fig. 4d,f,g). Thus, association

between the $\text{Ca}_\nu 1.2$ – $\text{Ca}_\nu \beta_3$ complex and the EMC pulls and twists various channel elements, mostly through rigid-body domain movements, that splay open the central pore.

Brace/crossbar helix is raised to an up position

A comparison with structures of the human EMC determined in lipid nanodiscs^{26,29} shows that $\text{Ca}_\nu 1.2$ – $\text{Ca}_\nu \beta_3$ binding causes a conformational change in the EMC luminal domain, comprising EMC1, EMC4, EMC7 and EMC10, in which the EMC top β -propeller domain moves by around 11.5 Å lateral to the membrane plane (Supplementary Fig. 9a–d). This tilt lifts and translates the EMC1 brace/crossbar helix towards the client by approximately 6 Å and 10 Å, respectively (Supplementary Fig. 9a–d and Supplementary Videos 10 and 11), enabling it to engage the VSD I–PD II interface (Fig. 1e) in an interaction that induces the folding of one helical turn at the brace/crossbar helix C-terminal end (residues Trp503–Tyr507) (Fig. 1e and Supplementary Fig. 9c,d). We designate this as the up conformation. The remainder of the EMC complex is largely unchanged, with the exception of clockwise rotations of the EMC3, EMC5 and EMC6 transmembrane elements (r.m.s.d._{Ca} = 1.44 Å, 0.91 Å and 0.63 Å for EMC3, EMC5 and EMC6, respectively) and a slight

counterclockwise repositioning of the EMC1 TM (r.m.s.d._{Ca} = 0.62 Å) (Supplementary Fig. 9b and Supplementary Video 12). By contrast, in the detergent complex lacking EMC7 (ref. 26), the luminal domain and brace/crossbar helix are in an up position similar to in the EMC–Ca_v1.2(ΔC)–Ca_vβ₃ complex (Supplementary Fig. 9e) (r.m.s.d._{Ca} = 0.84 Å), even though its C-terminal helical structure is shorter than that in the EMC–Ca_v1.2(ΔC)–Ca_vβ₃ complex and stops at Leu502. These conformational differences suggest that brace/crossbar helix engagement stabilizes the up position by biasing the apo-EMC conformational landscape. EMC1 up-state stabilization could enable endoplasmic reticulum lumen chaperones to recognize client-loaded EMCs and signal its holdase function, consistent with proposals that the different EMC conformations are associated with client-loaded states²⁶.

EMC and Ca_vα₂δ binding is mutually exclusive

Superposition of the EMC–Ca_v1.2(ΔC)–Ca_vβ₃ complex and Ca_v1.2–Ca_vβ₃–Ca_vα₂δ-1 shows that the EMC and Ca_vα₂δ interact with Ca_v1.2 in a mutually exclusive manner (Extended Data Fig. 7a). There are clashes with Ca_vα₂δ-1 all along the luminal parts of EMC1 as well as with the EMC1 brace/crossbar helix (Extended Data Fig. 7a,b). Notably, three EMC-bound Ca_v1.2 elements that are displaced from their positions in Ca_v1.2(ΔC)–Ca_vβ₃–Ca_vα₂δ-1, VSD I, PD II and PD III, each interact with Ca_vα₂δ in the fully assembled channel (Extended Data Fig. 7c). Rigid-body rotation of VSD I between its EMC-bound and Ca_vα₂δ-bound positions (Fig. 3a) moves Asp151 about 5 Å to complete the coordination sphere of the calcium ion bound to the Ca_vα₂δ von Willebrand factor type A (VWA) domain metal-ion-dependent adhesion site (MIDAS) (Extended Data Fig. 7c). This VSD I residue is conserved in Ca_v1s and Ca_v2s (Extended Data Fig. 3c) and its equivalent coordinates a similar Ca_vα₂δ-bound Ca²⁺ in Ca_v1.1 (ref. 43) and Ca_v2.2 (ref. 45). Ca_vα₂δ VWA MIDAS coordination of divalent ions is critical for Ca_vα₂δ binding to Ca_v1.2 (ref. 57) and Ca_v2.2 (ref. 58) and for the ability of Ca_vα₂δ to promote Ca_v1.2, Ca_v2.1 and Ca_v2.2 plasma membrane trafficking^{57–59}. We therefore denote this tripartite interaction as the divalent staple owing to its importance for assembled state stabilization.

Movement of PD II and PD III to their Ca_v1.2–Ca_vβ₃–Ca_vα₂δ-1 positions and restoration of PD intersubunit interactions (Fig. 3b and Extended Data Fig. 7d) appears to be linked to establishment of interactions with the Ca_vα₂δ VWA and Cache1 domains, respectively (Extended Data Fig. 7c), and agrees with the importance of PD III for Ca_vα₂δ binding⁶⁰. Notably, the large PD III extracellular loops linking PH1–IS5 and PH2–IS6 are disordered in the EMC–Ca_v1.2(ΔC)–Ca_vβ₃ complex but make extensive interactions with Ca_vα₂δ binding (Extended Data Fig. 7c), indicating that the folding of these elements is Ca_vα₂δ dependent. This interaction, together with divalent staple coordination, is central to the consolidation of the native Ca_v1.2–Ca_vβ₃–Ca_vα₂δ-1 assembly and suggests that the hand-off of the Ca_v1.2–Ca_vβ₃ complex from the EMC holdase to Ca_vα₂δ is a critical step in channel assembly.

Ca_vβ stabilizes Ca_vα₁ binding to the EMC

The strong association of the Ca_v1.2(ΔC)–Ca_vβ₃ complex and EMC (Extended Data Figs. 1a and 8a) prompted us to examine whether individual channel subunits could bind to the EMC. We expressed Ca_v1.2(ΔC) or Ca_vβ₃ and then performed a purification procedure similar to the one that yielded the EMC–Ca_v1.2(ΔC)–Ca_vβ₃ complex to assay EMC complex formation. Purified Ca_v1.2(ΔC) yielded a broader SEC peak than the EMC–Ca_v1.2(ΔC)–Ca_vβ₃ complex (Extended Data Fig. 8a,b) and contained EMC subunits identified by SDS-PAGE and MS (Extended Data Fig. 8b,c, Supplementary Fig. 1e,f and Supplementary Table 1a). A quantitative comparison found lower proportions of EMC subunits relative to Ca_v1.2(ΔC) than those observed for the EMC–Ca_v1.2(ΔC)–Ca_vβ₃ complex (Extended Data Fig. 8c), suggesting that Ca_v1.2(ΔC) binds to the EMC less tightly. By contrast, Ca_vβ₃ purification yielded

no EMC subunits (Extended Data Fig. 8d,e, Supplementary Fig. 1g and Supplementary Table 1a). This sample had two lower-molecular-mass bands corresponding to the Ca_vβ₃ nucleotide kinase and SH3 domains (Extended Data Fig. 8d and Supplementary Fig. 1g), which are known to associate^{40,61} and probably result from proteolytic cleavage. Thus, these data indicate that the Ca_v pore-forming subunit can stably associate with the EMC and that this association is strengthened by Ca_vβ binding, consistent with the multipoint nature of EMC–Ca_v1.2(ΔC)–Ca_vβ₃ interactions. Such interactions may explain the ability of Ca_vβ subunits to protect Ca_v1.2 (ref. 62) and Ca_v2.2 (ref. 63) pore-forming subunits from proteasome and ERAD pathway⁶² degradation in a variety of cell types, including neurons^{62,63}.

The Ca_v1.2 distal C-terminal tail affects forward trafficking⁶⁴. To test whether this region, absent from the EMC–Ca_v1.2(ΔC)–Ca_vβ₃ structure, might influence EMC binding, we expressed and purified the full-length Ca_v1.2–Ca_vβ₃ complex. Similar to the Ca_v1.2(ΔC) used in structure determination, this full-length subunit combination binds strongly to the EMC (Extended Data Fig. 8f,g, Supplementary Table 1b and Supplementary Fig. 1h), underscoring the biochemical stability of the EMC–Ca_v1.2–Ca_vβ₃ complex and further supporting the idea that this complex may be important for channel biogenesis.

EMC–Ca_v disruption compromises channel function

To test the idea that the EMC functions as a channel holdase, we designed Ca_v1.2 and Ca_vβ₃ mutants that perturbed the Ca_v1.2–TM dock and Ca_vβ–Cyto dock sites (Fig. 5a,b). These included a tri-Ala mutation of Ca_v1.2 residues making charge and cation–π interactions with the EMC1 TM dock site (R161A, I120A and W123A; Ca_v1.2(ΔC:3A)) (Fig. 5a), a penta-Ala Ca_vβ₃ mutant at the Cyto dock EMC2 site (M312A, L315A, T316A, M319A and D323A; Ca_vβ₃(5A)), a deletion of the Ca_vβ₃ loop that interacts with the EMC8 site (Ca_vβ₃(Δ220–240)) (Fig. 5b) and two mutants affecting both the EMC2 and EMC8 Cyto dock sites, an undeca-Ala Ca_vβ₃ mutant of all Cyto dock contacts (D220A, R226A, K234A, R240A, Q301A, R305A, M312A, L315A, T316A, M319A and D323A; Ca_vβ₃(11A)) (Fig. 5b) and a combination of the 5A and Δ220–240 mutants (Ca_vβ₃(5A:Δ220–240)) (Fig. 5b). We next examined the functional consequences using whole-cell recording of HEK293 cells transfected with various Ca_v1.2 and Ca_vβ₃ subunit combinations expressed with Ca_vα₂δ-1.

Disruption of interactions in the TM dock by Ca_v1.2(ΔC:3A) or the large EMC8 site by Ca_vβ₃(Δ220–240) reduced current levels by around 50% (Fig. 5c,d), whereas disruption of the smaller EMC2 site, Ca_vβ₃(5A), was not different from the control Ca_v1.2(ΔC)–Ca_vβ₃ pair. Notably, complete Cyto dock site disruption by Ca_vβ₃(5A:Δ220–240) or Ca_vβ₃(11A) reduced Ca_v currents by around 90% relative to the control, mirroring the effects of the absence Ca_vβ₃, of which the presence is essential for Ca_v plasma membrane expression^{5,10,11,62,65–67}. In all cases, the measurable channels had biophysical properties matching the parent Ca_v1.2(ΔC)–Ca_vβ₃ pair, with the exception of channels bearing Ca_vβ₃(Δ220–240) and Ca_vβ₃(5A:Δ220–240), which showed a small (around 7 mV) positive shift in activation voltage dependence (Extended Data Fig. 9a and Supplementary Table 2). Thus, these data indicate that EMC binding-site mutations affect channel function primarily by reducing plasma membrane expression and support the idea that the complex represents a productive step in functional Ca_v assembly.

We next purified Ca_v1.2(ΔC)–Ca_vβ₃(11A), a mutant that substantially reduced channel expression but spared channel biophysical properties (Extended Data Fig. 9a and Supplementary Table 2), and quantified its association with the EMC using MS (Extended Data Fig. 9b,c, Supplementary Fig. 1i,j and Supplementary Table 1c). These data show that ablation of the Cyto dock interactions greatly reduces (around 90%) EMC binding relative to Ca_v1.2(ΔC)–Ca_vβ₃ and matches the EMC-binding loss observed for Ca_v1.2(ΔC) in the absence of Ca_vβ₃ (Extended Data Fig. 8b,c). Taken together, the common effects that Ca_vβ Cyto dock site disruption or Ca_vβ absence have on EMC association and channel

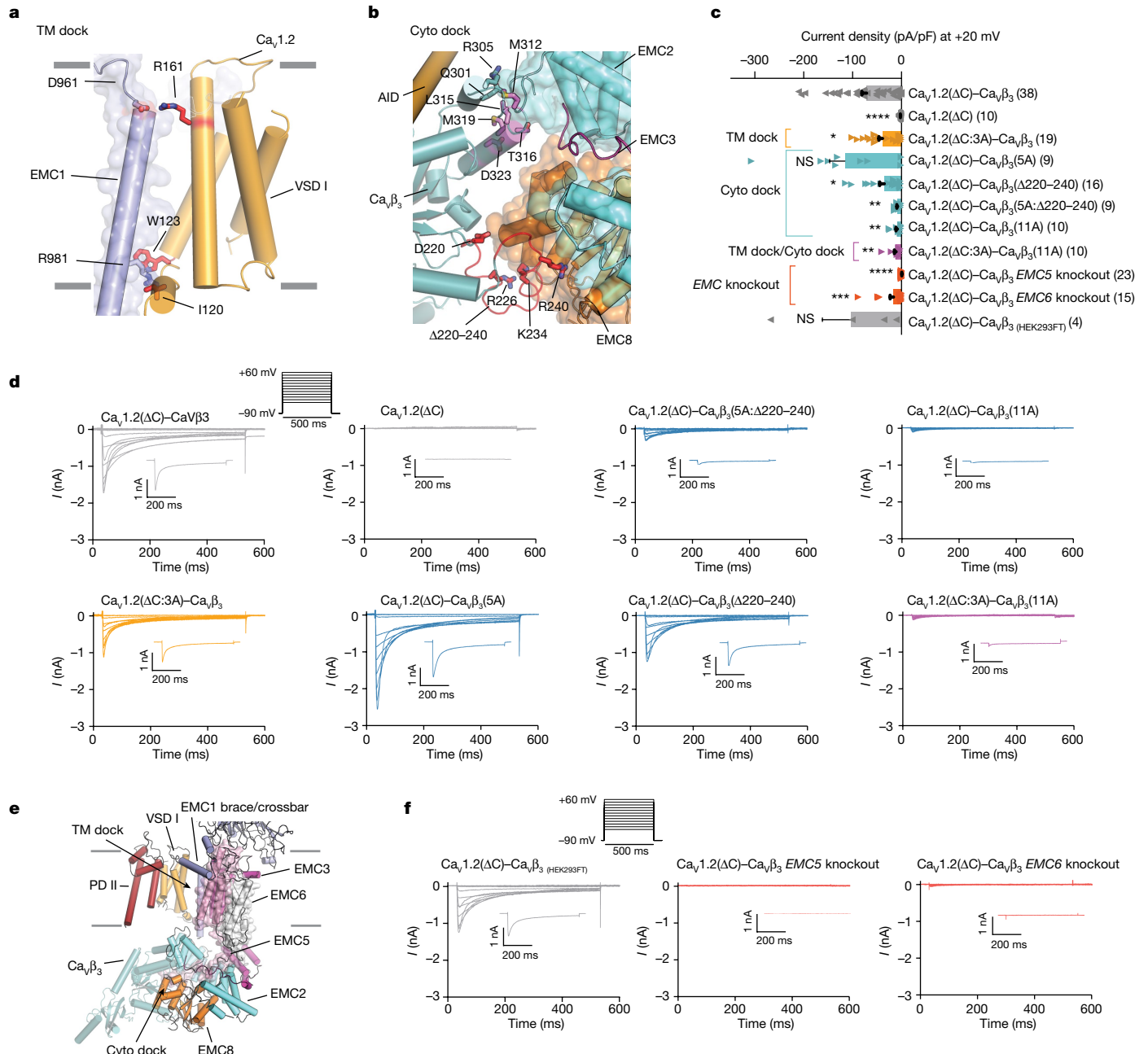


Fig. 5 | Disruption of EMC–channel interactions affects Ca_v function.

a, b, Cartoon diagrams showing the location of TM dock 3A mutants (**a**), and Cyto dock 5A (magenta), Δ220–240 (red) and 11A (sticks) mutants (**b**). **c**, Current densities at +20 mV for the indicated channels and HEK293FT cell lines. Data are mean ± s.e.m. The values in parentheses indicate n independent cells examined over ≥2 independent experiments. Statistical significance was assessed using two-sided unpaired t-tests between Ca_v1.2(ΔC)–Ca_vβ₃ and mutants. ***P < 0.0001, **P < 0.001, *P < 0.01, P = 0.01–0.05; NS, P > 0.05.

function (Fig. 5c and Extended Data Figs. 8a–e and 9b,c) indicate a key role of Ca_vβ–Cyto dock interactions in EMC–Ca_v complex formation and channel functional expression.

We next examined Ca_v function in HEK293 knockout cell lines lacking EMC subunits of which the absence disrupts the EMC²⁰. We tested cells lacking EMC5 (*EMC5 knockout*)^{20,68}, a transmembrane subunit that supports the EMC1 brace/crossbar helix that interacts with Ca_v1.2 and that scaffolds the Cyto dock EMC2 and EMC8 subunits; or EMC6 (*EMC6 knockout*)^{20,68}, a transmembrane subunit further from the EMC–Ca_v interface (Fig. 5e). Whole-cell recording (Fig. 5c,f) shows

d, Exemplar Ca²⁺ currents for HEK293 cells expressing the indicated channels in the presence of Ca_vα₂-δ-1. Insets: the stimulation protocol and currents at +20 mV. **e**, Cartoon of the EMC–Ca_v1.2(ΔC)–Ca_vβ₃ complex showing the following selected elements: EMC1, EMC2, EMC3, EMC5, EMC6, EMC8, Ca_v1.2 VSD I and PD II, and Ca_vβ₃. The arrows indicate the TM dock and Cyto dock. Surfaces are shown for EMC5 and EMC6. **f**, Exemplar Ca_v1.2(ΔC)–Ca_vβ₃–Ca_vα₂-δ-1 Ca²⁺ currents for HEK293FT and HEK293FT *EMC5*-knockout and *EMC6*-knockout cells. Insets: the protocol and currents at +20 mV.

that *EMC5* knockout (Fig. 5e) eliminates channel functional expression, whereas *EMC6* knockout partially suppresses channel functional expression. Importantly, channels expressed in *EMC6*-knockout cells were biophysically indistinguishable from channels expressed in unmodified HEK293 cells (Extended Data Fig. 9a and Supplementary Table 2), indicating that the loss of plasma membrane functional expression is a consequence of a loss of EMC–channel interactions and not a general effect. The ability of the EMC knockouts to phenocopy the effects of EMC–channel interface mutations together with the consequences of channel mutations in the EMC–Ca_v binding sites

Article

provides further evidence that the EMC and its interactions with the channel are essential for functional Ca_v expression.

Discussion

The profound effects that the intracellular $\text{Ca}_v\beta^5$ and extracellular $\text{Ca}_v\alpha_2\delta^{6,7}$ auxiliary subunits have on Ca_v1 and Ca_v2 function and trafficking are well known^{5,10–13,15}. Yet, apart from the role of the $\text{Ca}_v\beta$ –AID interaction in folding the $\text{Ca}_v\alpha_1$ AID helix^{41,69}, there is scant structural information regarding how $\text{Ca}_v\beta$ and $\text{Ca}_v\alpha_2\delta$ act during channel biogenesis and assembly. The identification of the EMC– $\text{Ca}_v1.2(\Delta C)$ – $\text{Ca}_v\beta_3$ complex, the evidence that $\text{Ca}_v1.2$ can bind to the EMC alone and the demonstration that EMC– Ca_v interactions affect functional channel expression offer direct insights into this process and suggest a mechanism by which the EMC acts as a holdase for the channel—a function that is probably relevant for diverse classes of membrane protein clients.

Various EMC domains have been suggested to function in transmembrane segment insertion into the lipid bilayer^{26,28,29,42} or serve as holdase sites²⁶. Notably, none of these elements form the TM dock and Cyto dock sites that bind to $\text{Ca}_v1.2(\Delta C)$ – $\text{Ca}_v\beta_3$, a membrane protein complex with a different topology compared with EMC tail-anchored protein clients⁹. Thus, our EMC-client structure expands the idea that the EMC uses diverse elements for different functions²⁶. The EMC1 TM dock uses a luminal-side salt bridge to an EMC1 residue implicated in client binding, Asp961 (ref. 30), and a cytoplasmic-side cation–π interaction³⁸ with EMC1 Arg981 (Extended Data Fig. 3a,b) to bind to the $\text{Ca}_v1.2$ VSD I (Fig. 1b–d and Extended Data Fig. 3a–c). The conserved nature of this interface strongly suggests that other Ca_v1 s and Ca_v2 s interact with the EMC. The observation that the $\text{Ca}_v\alpha_1$ subunit appears to bind to the EMC complex on its own (Extended Data Fig. 8b) suggests that EMC interactions with VSD I, the first channel transmembrane domain to be synthesized during translation^{2,18}, may be an early stabilization step during biogenesis. Augmentation of the TM dock site by VSD I and PD II interactions with the EMC1 brace/crossbar helix interactions that induce the up conformation of the EMC luminal subassembly (EMC1/4/7/10) (Supplementary Fig. 9a,c,d) may signal the client-loaded status of the EMC to luminal factors or other chaperones²⁶. Taken together, these findings define the TM dock as a hub of EMC holdase function.

$\text{Ca}_v\beta$ binding to the EMC Cyto dock involves EMC2 and EMC8 regions that were not to our knowledge previously known to bind to clients, and establishes the EMC intracellular domain as an important EMC-client interaction site. $\text{Ca}_v\beta$ interaction with the Cyto dock is critical for EMC binding (Extended Data Fig. 9b,c) and Ca_v functional expression (Fig. 5c,d), suggesting that EMC– Ca_v complex stabilization by $\text{Ca}_v\beta_3$ is a key step for functional channel formation. $\text{Ca}_v\beta$ binding to pore-forming $\text{Ca}_v\alpha_1$ subunits not only increases cell surface expression of Ca_v1 (refs. 62,65,66) and Ca_v2 (ref. 67) channels but also protects $\text{Ca}_v\alpha_1$ subunits from degradation by the proteasome⁶³ and the ERAD pathway⁶². Taken together, these observations suggest the EMC–channel complex protects the partly assembled channel from degradation and points to a new mechanism by which $\text{Ca}_v\beta$ binding influences the fate of $\text{Ca}_v\alpha_1$ subunits.

The most substantial structural consequence of the EMC– $\text{Ca}_v\beta$ interaction is the orchestration of the coordinated displacement of $\text{Ca}_v1.2$ pore-forming subunit AID, VSD II and PD III elements in a manner that causes partial extraction of PD III from the channel pore (Fig. 3a, Extended Data Fig. 5b and Supplementary Videos 2 and 3). Together with the rotation of VSD I away from its native position, these changes substantially reshape the extracellular portions of the channel adjacent to the EMC relative to their conformations in the $\text{Ca}_v1.2(\Delta C)$ – $\text{Ca}_v\beta_3$ – $\text{Ca}_v\alpha_2\delta$ -1 complex. As the EMC and $\text{Ca}_v\alpha_2\delta$ -1 bind to the same side of the $\text{Ca}_v\alpha$ – $\text{Ca}_v\beta$ core in a mutually exclusive manner (Extended Data Fig. 7a), these conformational changes suggest that the role of the EMC is to prepare the $\text{Ca}_v\alpha$ – $\text{Ca}_v\beta$ complex for $\text{Ca}_v\alpha_2\delta$ binding.

Association of $\text{Ca}_v\alpha_2\delta$ with the pore-forming subunit channel is governed by $\text{Ca}_v\alpha_2\delta$ VWA MIDAS Ca^{2+} binding during a step that is thought to occur in the endoplasmic reticulum lumen⁵⁹ and is crucial for trafficking^{17,70}. In agreement with these observations, our structural data point to a central role for the divalent staple that bridges the $\text{Ca}_v\alpha_2\delta$ VWA MIDAS domain and VSD I in the transition between the EMC-bound and $\text{Ca}_v\alpha_2\delta$ -bound complexes. The structures show that $\text{Ca}_v\alpha$ – $\text{Ca}_v\beta$ complex hand-off from the EMC to $\text{Ca}_v\alpha_2\delta$ involves a rigid body rotation of VSD I that enables the conserved Asp151, which is crucial for $\text{Ca}_v\alpha_2\delta$ -dependent Ca_v1 (ref. 57) and Ca_v2 (ref. 58) trafficking, to complete the divalent staple coordination sphere (Extended Data Figs. 3c and 7c) and stabilize interaction with $\text{Ca}_v\alpha_2\delta$. In agreement with the importance of PD III in $\text{Ca}_v\alpha_2\delta$ binding⁶⁰, such an exchange would permit the extracellular PD III loops that are disordered in the EMC– $\text{Ca}_v1.2$ – $\text{Ca}_v\beta_3$ complex to form extensive interactions with $\text{Ca}_v\alpha_2\delta$ VWA and CacheL domains (Extended Data Fig. 7c). Establishing native $\text{Ca}_v\alpha_2\delta$ interactions with PD III would require $\text{Ca}_v\beta$ release from the Cyto-dock and expulsion of the lipid plug (Fig. 4d,f,g) as the pore closes. Whether such steps happen in an ordered manner or in an EMC– $\text{Ca}_v\alpha_2\delta$ capture–release competition are important unanswered questions. Taken together, our data strongly suggest that the extensive conserved interactions of $\text{Ca}_v\alpha$ and $\text{Ca}_v\beta$ subunits with the EMC have a role in the ability of $\text{Ca}_v\alpha_2\delta$ to promote trafficking of Ca_v1 s and Ca_v2 s^{10,13,71}, indicate that this exchange is a key step in channel biogenesis and quality control, and provide a framework to study Ca_v biogenesis. Exchange between the EMC holdase and $\text{Ca}_v\alpha_2\delta$ is likely also to be influenced by Ca_v domains that enhance forward trafficking⁶⁴, Ca_v -directed drugs^{6,7,33}, especially the gabapentinoids that target $\text{Ca}_v\alpha_2\delta$ ^{14,16,17}, and Ca_v subunit disease mutations^{4,5,34}. These factors require further investigation.

The EMC is linked to the biogenesis of a variety of ion channels^{21–23}, including one VGIC superfamily member²². Given the conserved structure of VSD within the VGIC superfamily¹, the EMC may participate in the biogenesis of other VGICs through TM dock interactions similar to those defined here. By contrast, binding of the Cyto dock site involves a unique Ca_v1 and Ca_v2 subunit, $\text{Ca}_v\beta^5$. Interaction with this part of the EMC largely involves a $\text{Ca}_v\beta$ loop structure that is important for EMC-dependent functional expression (Fig. 5) and could have structural equivalents in other proteins. Defining the roles of the TM and Cyto dock sites for binding to Ca_v s and other clients is an important line of study enabled by the framework presented here. It will also be essential to test whether other classes of clients engage these newly defined sites or interact with other, yet to be defined, EMC client-binding sites. Furthermore, many VGICs bear disease mutations that are not easily rationalized based on mature channel structure. Some of these mutations may disturb EMC interactions that are crucial for channel assembly, maturation and quality control. The structural framework described here sets the stage for detailed mechanistic studies into the structural basis of trafficking and assembly of VGICs and other membrane proteins that are thought to interact with the EMC⁹.

Online content

Any methods, additional references, Nature Portfolio reporting summaries, source data, extended data, supplementary information, acknowledgements, peer review information; details of author contributions and competing interests; and statements of data and code availability are available at <https://doi.org/10.1038/s41586-023-06175-5>.

1. Catterall, W. A., Wischedahl, G. & Zheng, N. The chemical basis for electrical signaling. *Nat. Chem. Biol.* **13**, 455–463 (2017).
2. Isacoff, E. Y., Jan, L. Y. & Minor Jr., D. L. Conduits of life's spark: a perspective on ion channel research since the birth of neuron. *Neuron* **80**, 658–674 (2013).
3. Zamponi, G. W., Strieussig, J., Koschak, A. & Dolphin, A. C. The physiology, pathology, and pharmacology of voltage-gated calcium channels and their future therapeutic potential. *Pharmacol. Rev.* **67**, 821–870 (2015).
4. Nanou, E. & Catterall, W. A. Calcium channels, synaptic plasticity, and neuropsychiatric disease. *Neuron* **98**, 466–481 (2018).

5. Buraei, Z. & Yang, J. The β subunit of voltage-gated Ca^{2+} channels. *Physiol. Rev.* **90**, 1461–1506 (2010).
6. Dooley, D. J., Taylor, C. P., Donevan, S. & Feltner, D. Ca^{2+} channel $\alpha_2\delta$ ligands: novel modulators of neurotransmission. *Trends Pharmacol. Sci.* **28**, 75–82 (2007).
7. Dolphin, A. C. Voltage-gated calcium channels and their auxiliary subunits: physiology and pathophysiology and pharmacology. *J. Physiol.* **594**, 5369–5390 (2016).
8. Jonikas, M. C. et al. Comprehensive characterization of genes required for protein folding in the endoplasmic reticulum. *Science* **323**, 1693–1697 (2009).
9. Hegde, R. S. The function, structure, and origins of the ER membrane protein complex. *Annu. Rev. Biochem.* **91**, 651–678 (2022).
10. Shistik, E., Ivanina, T., Puri, T., Hosey, M. & Dascal, N. Ca^{2+} current enhancement by $\alpha_2\delta$ and β subunits in *Xenopus* oocytes: contribution of changes in channel gating and $\alpha 1$ protein level. *J. Physiol.* **489**, 55–62 (1995).
11. Singer, D. et al. The roles of the subunits in the function of the calcium channel. *Science* **253**, 1553–1557 (1991).
12. Gurnett, C. A., De Waard, M. & Campbell, K. P. Dual function of the voltage-dependent Ca^{2+} channel $\alpha_2\delta$ subunit in current stimulation and subunit interaction. *Neuron* **16**, 431–440 (1996).
13. Davies, A. et al. Functional biology of the $\alpha_2\delta$ subunits of voltage-gated calcium channels. *Trends Pharmacol. Sci.* **28**, 220–228 (2007).
14. Field, M. J. et al. Identification of the $\alpha_2\delta-1$ subunit of voltage-dependent calcium channels as a molecular target for pain mediating the analgesic actions of pregabalin. *Proc. Natl Acad. Sci. USA* **103**, 17537–17542 (2006).
15. Dolphin, A. C. Voltage-gated calcium channel $\alpha_2\delta$ subunits: an assessment of proposed novel roles. *F1000Res* <https://doi.org/10.12688/f1000research.16104.1> (2018).
16. Bauer, C. S. et al. The increased trafficking of the calcium channel subunit $\alpha_2\delta-1$ to presynaptic terminals in neuropathic pain is inhibited by the $\alpha_2\delta$ ligand pregabalin. *J. Neurosci.* **29**, 4076–4088 (2009).
17. Cassidy, J. S., Ferron, L., Kadurin, I., Pratt, W. S. & Dolphin, A. C. Functional exofacially tagged N-type calcium channels elucidate the interaction with auxiliary $\alpha_2\delta-1$ subunits. *Proc. Natl Acad. Sci. USA* **111**, 8979–8984 (2014).
18. Deutsch, C. The birth of a channel. *Neuron* **40**, 265–276 (2003).
19. Christianson, J. C. et al. Defining human ERAD networks through an integrative mapping strategy. *Nat. Cell Biol.* **14**, 93–105 (2011).
20. Guna, A., Volkmar, N., Christianson, J. C. & Hegde, R. S. The ER membrane protein complex is a transmembrane domain insertase. *Science* **359**, 470–473 (2018).
21. Richard, M., Boulin, T., Robert, V. J., Richmond, J. E. & Bessereau, J. L. Biosynthesis of ionotropic acetylcholine receptors requires the evolutionarily conserved ER membrane complex. *Proc. Natl Acad. Sci. USA* **110**, E1055–E1063 (2013).
22. Talbot, B. E., Vandorpe, D. H., Stotter, B. R., Alper, S. L. & Schlendorff, J. S. Transmembrane insertases and N-glycosylation critically determine synthesis, trafficking, and activity of the nonselective cation channel TRPC6. *J. Biol. Chem.* **294**, 12655–12669 (2019).
23. Coelho, J. P. L. et al. A network of chaperones prevents and detects failures in membrane protein lipid bilayer integration. *Nat. Commun.* **10**, 672 (2019).
24. Satoh, T., Ohba, A., Liu, Z., Inagaki, T. & Satoh, A. K. dPob/EMC is essential for biosynthesis of rhodopsin and other multi-pass membrane proteins in *Drosophila* photoreceptors. *eLife* **4**, e06306 (2015).
25. Chitwood, P. J., Juszkiewicz, S., Guna, A., Shao, S. & Hegde, R. S. EMC is required to initiate accurate membrane protein topogenesis. *Cell* **175**, 1507–1519 (2018).
26. Miller-Vedam, L. E. et al. Structural and mechanistic basis of the EMC-dependent biogenesis of distinct transmembrane clients. *eLife* **9**, e62611 (2020).
27. Shurtliff, M. J. et al. The ER membrane protein complex interacts cotranslationally to enable biogenesis of multipass membrane proteins. *eLife* **7**, e37018 (2018).
28. O'Donnell, J. P. et al. The architecture of EMC reveals a path for membrane protein insertion. *eLife* **9**, e57887 (2020).
29. Pleiner, T. et al. Structural basis for membrane insertion by the human ER membrane protein complex. *Science* **369**, 433–436 (2020).
30. Bagchi, P., Inoue, T. & Tsai, B. EMC1-dependent stabilization drives membrane penetration of a partially destabilized non-enveloped virus. *eLife* **5**, e21470 (2016).
31. Hofmann, F., Flockerzi, V., Kahl, S. & Wegener, J. W. L-type $\text{Ca}_{v}1.2$ calcium channels: from *in vitro* findings to *in vivo* function. *Physiol. Rev.* **94**, 303–326 (2014).
32. Hullin, R. et al. Cardiac L-type calcium channel β -subunits expressed in human heart have differential effects on single channel characteristics. *J. Biol. Chem.* **278**, 21623–21630 (2003).
33. Zamponi, G. W. Targeting voltage-gated calcium channels in neurological and psychiatric diseases. *Nat. Rev. Drug Discov.* **15**, 19–34 (2016).
34. Marcantoni, A., Calorio, C., Hidisoglu, E., Chiantia, G. & Carbone, E. $\text{Ca}_{v}1.2$ channelopathies causing autism: new hallmarks on Timothy syndrome. *Pflügers Arch.* **472**, 775–789 (2020).
35. Chen, Z., Mondal, A. & Minor Jr. D. L. Structural basis for $\text{Ca}_{v}\alpha_2\delta$: gabapentin binding. *Nat. Struct. Mol. Biol.* <https://doi.org/10.1038/s41594-023-00951-7> (2023).
36. Kozai, D. et al. Recognition mechanism of a novel gabapentinoid drug, mirogabalin, for recombinant human $\alpha_2\delta-1$, a voltage-gated calcium channel subunit. *J. Mol. Biol.* **435**, 168049 (2023).
37. Dooley, D. J., Donovan, C. M., Meder, W. P. & Whetzel, S. Z. Preferential action of gabapentin and pregabalin at P/Q-type voltage-sensitive calcium channels: inhibition of K^{+} -evoked [^3H]-norepinephrine release from rat neocortical slices. *Synapse* **45**, 171–190 (2002).
38. Infield, D. T. et al. Cation– π Interactions and their functional roles in membrane proteins. *J. Mol. Biol.* **433**, 167035 (2021).
39. Chen, Y. H. et al. Structural basis of the $\alpha 1\beta$ subunit interaction of voltage-gated Ca^{2+} channels. *Nature* **429**, 675–680 (2004).
40. Van Petegem, F., Clark, K. A., Chatelain, F. C. & Minor Jr. D. L. Structure of a complex between a voltage-gated calcium channel β -subunit and an α -subunit domain. *Nature* **429**, 671–675 (2004).
41. Van Petegem, F., Duderstadt, K. E., Clark, K. A., Wang, M. & Minor Jr. D. L. Alanine-scanning mutagenesis defines a conserved energetic hotspot in the $\text{Ca}_{v}\alpha_1$ –AID– $\text{Ca}_{v}\beta$ interaction site that is critical for channel modulation. *Structure* **16**, 280–294 (2008).
42. Bai, L., You, Q., Feng, X., Kovach, A. & Li, H. Structure of the ER membrane complex, a transmembrane-domain insertase. *Nature* **584**, 475–478 (2020).
43. Wu, J. et al. Structure of the voltage-gated calcium channel $\text{Ca}_{v}1.1$ at 3.6 Å resolution. *Nature* **537**, 191–196 (2016).
44. Yao, X., Gao, S. & Yan, N. Structural basis for pore blockade of human voltage-gated calcium channel $\text{Ca}_{v}1.3$ by motion sickness drug cinnarizine. *Cell Res.* <https://doi.org/10.1038/s41422-022-00663-5> (2022).
45. Gao, S., Yao, X. & Yan, N. Structure of human $\text{Ca}_{v}2.2$ channel blocked by the painkiller ziconotide. *Nature* **596**, 143–147 (2021).
46. Zhao, Y. et al. Cryo-EM structures of apo and antagonist-bound human $\text{Ca}_{v}3.1$. *Nature* **576**, 492–497 (2019).
47. Brown, J. P., Dissanayake, V. U., Briggs, A. R., Milic, M. R. & Gee, N. S. Isolation of the [^3H] gabapentin-binding protein/ $\alpha_2\delta$ Ca^{2+} channel subunit from porcine brain: development of a radioligand binding assay for $\alpha_2\delta$ subunits using [^3H]-leucine. *Anal. Biochem.* **255**, 236–243 (1998).
48. Dolphin, A. C. Calcium channel auxiliary $\alpha_2\delta$ and beta subunits: trafficking and one step beyond. *Nat. Rev. Neurosci.* **13**, 542–555 (2012).
49. Wu, J. et al. Structure of the voltage-gated calcium channel $\text{Ca}_{v}1.1$ complex. *Science* **350**, aad2395 (2015).
50. Gumerov, V. M. et al. Amino acid sensor conserved from bacteria to humans. *Proc. Natl Acad. Sci. USA* **119**, e2110415119 (2022).
51. Wang, M., Offord, J., Oxender, D. L. & Su, T. Z. Structural requirement of the calcium-channel subunit $\alpha_2\delta$ for gabapentin binding. *Biochem. J.* **342**, 313–320 (1999).
52. Zhao, Y. et al. Molecular basis for ligand modulation of a mammalian voltage-gated Ca^{2+} Channel. *Cell* **177**, 1495–1506 (2019).
53. He, L. et al. Structure, gating, and pharmacology of human $\text{Ca}_{v}3.3$ channel. *Nat. Commun.* **13**, 2084 (2022).
54. Gao, S. & Yan, N. Structural basis of the modulation of the voltage-gated calcium ion channel $\text{Ca}_{v}1.1$ by dihydropyridine compounds. *Angew. Chem. Int. Ed. Engl.* **60**, 3131–3137 (2021).
55. Tao, X., Lee, A., Limapichat, W., Dougherty, D. A. & MacKinnon, R. A gating charge transfer center in voltage sensors. *Science* **328**, 67–73 (2010).
56. Arrigoni, C. et al. Quaternary structure independent folding of voltage-gated ion channel pore domain subunits. *Nat. Struct. Mol. Biol.* **29**, 537–548 (2022).
57. Bourdin, B., Briot, J., Tetreault, M. P., Sauve, R. & Parent, L. Negatively charged residues in the first extracellular loop of the L-type $\text{Ca}_{v}1.2$ channel anchor the interaction with the $\text{Ca}_{v}\alpha_2\delta 1$ auxiliary subunit. *J. Biol. Chem.* **292**, 17236–17249 (2017).
58. Dahimene, S. et al. The $\alpha_2\delta$ -like protein Cachd1 increases N-type calcium currents and cell surface expression and competes with $\alpha_2\delta-1$. *Cell Rep.* **25**, 1610–1621 (2018).
59. Canti, C. et al. The metal-ion-dependent adhesion site in the Von Willebrand factor-A domain of $\alpha_2\delta$ subunits is key to trafficking voltage-gated Ca^{2+} channels. *Proc. Natl Acad. Sci. USA* **102**, 11230–11235 (2005).
60. Gurnett, C. A., Felix, R. & Campbell, K. P. Extracellular interaction of the voltage-dependent Ca^{2+} channel $\alpha_2\delta$ and α_1 subunits. *J. Biol. Chem.* **272**, 18508–18512 (1997).
61. Opatowsky, Y., Chomsky-Hecht, O., Kang, M. G., Campbell, K. P. & Hirsch, J. A. The voltage-dependent calcium channel β subunit contains two stable interacting domains. *J. Biol. Chem.* **278**, 52323–52332 (2003).
62. Altier, C. et al. The $\text{CaV}\beta$ subunit prevents RFP2-mediated ubiquitination and proteasomal degradation of L-type channels. *Nat. Neurosci.* **14**, 173–180 (2011).
63. Waithe, D., Ferron, L., Page, K. M., Chaggard, K. & Dolphin, A. C. β -Subunits promote the expression of $\text{Ca}_{v}2.2$ channels by reducing their proteasomal degradation. *J. Biol. Chem.* **286**, 9598–9611 (2011).
64. Fang, K. & Colecraft, H. M. Mechanism of auxiliary β -subunit-mediated membrane targeting of L-type ($\text{Ca}_{v}1.2$) channels. *J. Physiol.* **589**, 4437–4455 (2011).
65. Altier, C. et al. Trafficking of L-type calcium channels mediated by the postsynaptic scaffolding protein AKAP79. *J. Biol. Chem.* **277**, 33598–33603 (2002).
66. Obermair, G. J. et al. Reciprocal interactions regulate targeting of calcium channel beta subunits and membrane expression of α_1 subunits in cultured hippocampal neurons. *J. Biol. Chem.* **285**, 5776–5791 (2010).
67. Leroy, J. et al. Interaction via a key tryptophan in the I-II linker of N-type calcium channels is required for $\beta 1$ but not for palmitoylated $\beta 2$, implicating an additional binding site in the regulation of channel voltage-dependent properties. *J. Neurosci.* **25**, 6984–6996 (2005).
68. Pleiner, T. et al. A selectivity filter in the ER membrane protein complex limits protein misinsertion at the ER. *J. Cell Biol.* **222**, e202212007 (2023).
69. Opatowsky, Y., Chen, C. C., Campbell, K. P. & Hirsch, J. A. Structural analysis of the voltage-dependent calcium channel β subunit functional core and its complex with the $\alpha 1$ interaction domain. *Neuron* **42**, 387–399 (2004).
70. Dolphin, A. C. & Lee, A. Presynaptic calcium channels: specialized control of synaptic neurotransmitter release. *Nat. Rev. Neurosci.* **21**, 213–229 (2020).
71. Felix, R., Gurnett, C. A., De Waard, M. & Campbell, K. P. Dissection of functional domains of the voltage-dependent Ca^{2+} channel $\alpha_2\delta$ subunit. *J. Neurosci.* **17**, 6884–6891 (1997).
72. Smart, O. S., Neduvilil, J. G., Wang, X., Wallace, B. A. & Sansom, M. S. HOLE: a program for the analysis of the pore dimensions of ion channel structural models. *J. Mol. Graph.* **14**, 354–360 (1996).
73. Pravda, L. et al. MOLEonline: a web-based tool for analyzing channels, tunnels and pores (2018 update). *Nucleic Acids Res.* **46**, W368–W373 (2018).

Publisher's note Springer Nature remains neutral with regard to jurisdictional claims in published maps and institutional affiliations.

Springer Nature or its licensor (e.g. a society or other partner) holds exclusive rights to this article under a publishing agreement with the author(s) or other rightsholder(s); author self-archiving of the accepted manuscript version of this article is solely governed by the terms of such publishing agreement and applicable law.

© The Author(s), under exclusive licence to Springer Nature Limited 2023

Article

Methods

Expression and purification of human $\text{Ca}_v1.2$ and $\text{Ca}_v1.2$ -loaded human EMC complex

Codon-optimized cDNAs of human $\text{Ca}_v1.2$ (full length) (2,138 residues; UniProt: Q13936-20); human $\text{Ca}_v1.2$ bearing a C-terminal truncation at residue 1648 ($\text{Ca}_v1.2(\Delta\text{C})$), a site 13 residues after the end of the IQ domain ($\Delta1649-2138$; UniProt: Q13936-20, 1,648 residues) followed by a 3C protease cleavage site, monomeric enhanced green fluorescent protein (mEGFP) and a His₈ tag; rabbit $\text{Ca}_v\alpha_2\delta-1$ (1,105 residues; UniProt: P13806-1); and rabbit $\text{Ca}_v\beta_3$ (477 residues; UniProt: P54286) followed by a Strep-tag II sequence⁷⁴ were synthesized (GenScript) and each was subcloned into a modified pFastBac expression vector in which the polyhedrin promoter was replaced with a mammalian cell active CMV promoter⁷⁵. The expression vector for $\text{Ca}_v\beta_3(11A)$ was generated by site-directed mutagenesis in pFastBac. All of the constructs were sequenced completely. The Strep-tag-bearing rabbit $\text{Ca}_v\beta_3$ construct was used to generate a stable cell line in HEK293S GnT⁻ (ATCC) using a lentiviral system as described previously⁷⁶ and denoted as $\text{Ca}_v\beta_3$ -stable.

Chemically competent DH10EmBacY (Geneva Biotech) cells were used to generate the recombinant bacmid DNA, which was then used to transfect *Spodoptera frugiperda* (Sf9) cells to make baculoviruses for each subunit⁷⁷. For structural and biochemical studies, $\text{Ca}_v1.2$ (full length) and $\text{Ca}_v1.2(\Delta\text{C})$ were expressed in $\text{Ca}_v\beta_3$ -stable cells alone or together with $\text{Ca}_v\alpha_2\delta-1$ using a baculovirus transduction-based system⁷⁷. For pull-down studies, $\text{Ca}_v1.2$, $\text{Ca}_v\beta_3$ or both were expressed in unmodified HEK293S GnT⁻ cells. $\text{Ca}_v\beta_3$ -stable and HEK293S GnT⁻ cells were grown in suspension at 37 °C supplied with 8% CO₂ in FreeStyle 293 Expression Medium (Gibco) supplemented with 2% fetal bovine serum (Peak Serum), and were transduced with 5% (v/v) baculovirus for each target subunit when the cell density reached around 2.5×10^6 cells per ml. Sodium butyrate (10 mM) was added to cell culture 16–24 h after transduction and the cells were subsequently grown at 30 °C. Cells were collected 48 h after transduction by centrifugation at 5,000g for 30 min. The pellet was washed with Dulbecco's phosphate-buffered saline (Gibco) and stored at -80 °C.

A cell pellet (from around 3.6 l culture) was resuspended in 200 ml of resuspension buffer containing 0.3 M sucrose, 1 mM ethylenediaminetetraacetic acid, 10 mM Tris-HCl, pH 8.0 supplemented with 1 mM phenylmethylsulfonyl fluoride and 4 Pierce protease inhibitor tablets (Thermo Fisher Scientific), then stirred gently on the Variomag magnetic stirrer MONO DIRECT (Thermo Fisher Scientific) at 4 °C for 30 min. The membrane fraction was collected by centrifugation at 185,500g for 1 h and subsequently solubilized in 200 ml of solubilization buffer (buffer S) containing 500 mM NaCl, 5% glycerol (v/v), 0.5 mM CaCl₂, 20 mM Tris-HCl, pH 8.0, supplemented with 1% (w/v) GDN, and rotated on the Orbitron rotator II (speed mode S) (Boekel Scientific) at 4 °C for 2 h. The supernatant, collected by centrifugation at 185,500g for 1 h, was diluted with an equal volume of buffer S to a final concentration of 0.5% GDN and incubated with anti-GFP nanobody Sepharose resin⁷⁸ at 4 °C overnight. The resin was loaded onto an Econo-Column chromatography column (BioRad) and then was then washed stepwise with 20 column volumes (CV) of buffer S supplemented with 0.1% (w/v) GDN, 20 CV of buffer S supplemented with 0.02% (w/v) GDN, and 20 CV of elution buffer (buffer E) containing 150 mM NaCl, and 0.5 mM CaCl₂, 0.02% (w/v) GDN 20 mM, Tris-HCl pH 8.0. The protein was eluted with 3C protease⁷⁹ and subsequently incubated at 4 °C for 2 h with 4 ml of Strep-tactin Superflow Plus beads (Qiagen) pre-equilibrated with buffer E. The beads were washed with 20 CV of buffer E and the protein was eluted with buffer E supplemented with 2.5 mM desthiobiotin. The eluent was concentrated using an Amicon Ultra-15 100-kDa cut-off centrifugal filter unit (Merck Millipore) before purification using the Superose 6 Increase 10/300 GL gel filtration column (GE Healthcare) pre-equilibrated in buffer E. Peak fractions were pooled for MS analysis and concentrated using the Amicon Ultra 0.5 ml 100 kDa cut-off

centrifugal filter unit (Merck Millipore) for cryo-EM sample preparation (1.7 mg ml⁻¹ $\text{Ca}_v1.2(\Delta\text{C})$ – $\text{Ca}_v\beta_3$ sample or 2.7 mg ml⁻¹ $\text{Ca}_v1.2(\Delta\text{C})$ – $\text{Ca}_v\beta_3$ – $\text{Ca}_v\alpha_2\delta-1$ sample).

Two-electrode voltage-clamp electrophysiology

The C-terminally truncated human $\text{Ca}_v1.2(\Delta1649-2138)$ – $\text{Ca}_v1.2(\Delta\text{C})$ construct was obtained from a full-length human $\text{Ca}_v1.2$ (UniProt: Q13936-20) template in pcDNA3.1 (Invitrogen) using the Gibson Assembly kit (NEB). Full-length $\text{Ca}_v1.2$ or $\text{Ca}_v1.2(\Delta\text{C})$ was co-expressed with rabbit $\text{Ca}_v\beta_3$ (UniProt: P54286) in pcDNA3.1 for *Xenopus* oocyte two-electrode voltage-clamp experiments. A total of 5 µg of $\text{Ca}_v1.2$ or $\text{Ca}_v1.2(\Delta\text{C})$ and $\text{Ca}_v\beta_3$ cDNA was linearized using 30 U of the restriction enzymes XhoI and NotI (NEB), respectively, at 37 °C overnight. The linearized cDNA was used as the template to synthesize capped mRNA using the T7 mMessenger kit (Ambion). A total of 100 nl of $\text{Ca}_v1.2$ or $\text{Ca}_v1.2(\Delta\text{C})$ and $\text{Ca}_v\beta_3$ mixed at a 1:1 molar ratio was injected into *Xenopus* oocytes 1–2 days before recording. Two-electrode voltage-clamp experiments were performed as previously described⁸⁰. In brief, oocytes were injected with 50 nl of 100 mM BAPTA 2–4 min before recording to minimize calcium-activated chloride currents^{80,81}. For recording of Ca²⁺ or Ba²⁺ currents, bath solutions contained 50 mM NaOH, 40 mM Ca(NO₃)₂ or 40 mM Ba(OH)₂, respectively, 1 mM KOH, 10 mM HEPES, adjusted to pH 7.4 with HNO₃. Electrodes were filled with 3 M KCl and had resistances of 0.3–1.0 MΩ. Recordings were conducted at room temperature from a holding potential of -90 mV. Leak currents were subtracted using a P/4 protocol.

Oocytes were collected from female *Xenopus laevis* (Nasco, LM00531) and housed in the UCSF Laboratory Animal Resource Center (LARC) facilities. The use of these *Xenopus* oocytes was approved by IACUC (protocol approval, AN193390-01B) and experiments were performed in accordance with University of California guidelines and regulations.

Whole-cell patch-clamp electrophysiology

Whole-cell patch-clamp experiments were performed as previously described⁸⁰ using pcDNA3.1 vectors for $\text{Ca}_v1.2$ (UniProt: Q13936-20) and rabbit $\text{Ca}_v\alpha_2\delta-1$ (UniProt: P13806-1)⁸⁰, and pTracer-CMV2-GFP (Thermo Fisher Scientific, V88520) for rabbit $\text{Ca}_v\beta_3$ (UniProt: P54286). $\text{Ca}_v1.2$ and $\text{Ca}_v\beta_3$ mutants were generated by site-directed mutagenesis. Human embryonic kidney cells (HEK293, ATCC, CRL-1573) and HEK293FT cell lines^{20,68} (WT, *EMC5* knockout and *EMC6* knockout) were grown at 37 °C under 5% CO₂ in a Dulbecco's modified Eagle's medium supplemented with 10% fetal bovine serum, 1% L-glutamine, 1% (v/v) GlutaMAX, 1% (v/v) sodium pyruvate, 1% (v/v) MEM non-essential amino acids and antibiotics (100 IU ml⁻¹ penicillin and 100 mg ml⁻¹ streptomycin). HEK293 cells and HEK293FT cells were transfected (in 35 mm diameter wells of Corning 6-well flat-bottom culture plates) with Lipofectamine 2000 (Invitrogen) and plated onto coverslips coated with Matrigel (BD Biosciences).

Cells were transfected using a total of 4.6 µg DNA with a ratio by weight of 2:0.9:1.3:0.4 of $\text{Ca}_v\alpha_1$; $\text{Ca}_v\beta_3$; $\text{Ca}_v\alpha_2\delta-1$:sv40 T-antigen plasmids. The SV40 T-antigen plasmid was used to increase channel expression. Transfected cells were identified visually using enhanced green fluorescent protein (eGFP) expression in the second cassette of the plasmid expressing the β_3 subunit. Whole-cell patch-clamp⁸² was used to record Ca²⁺ currents at room temperature (23 ± 2 °C) 36–72 h after transfection. Data acquisition was performed using pCLAMP 9 (Molecular Devices) and an Axopatch 200B amplifier (Molecular Devices). Pipettes were pulled from borosilicate glass capillaries (TW150F-3; World Precision Instruments) and polished (MF-900 Microforge; Narishige) to obtain 2–3 MΩ resistances. 40–60% of the voltage error due to the series resistance was compensated, and leak currents were subtracted using a P/4 protocol. For $\text{Ca}_v1.2$ experiments, the pipette solution contained 120 mM NMDG, 1 mM MgCl₂, 5 mM EGTA, 4 mM Mg-ATP, 42 mM HEPES (pH 7.3 adjusted with methane sulfonic acid). The bath solution contained 40 mM CaCl₂, 1 mM MgCl₂, 105 mM Tris (pH 7.3 adjusted with

methane sulfonic acid). Statistical significance was assessed using Student's *t*-tests or Mann–Whitney *U*-tests as appropriate.

Data quantification and statistical analysis

All of the details of data analysis and statistical analysis are provided in the Methods and the figure legends. All results are from at least two independent oocyte batches or two independent HEK293 transfections. Data were acquired using Clampex 11.2 (Molecular Devices) and analysed with Clampfit 10.6 (Axon Instruments). Activation curves were obtained by fitting the data (GraphPad Prism) with the following Boltzmann equation: $Y = Y_{\min} + (Y_{\max} - Y_{\min})/(1 + \exp((V_{1/2} - V_m)/k))$, where $V_{1/2}$ is the midpoint of activation, k is the slope factor of the activation curve, $Y = G/G_{\max}$ and Y_{\max} and Y_{\min} are the maximum and minimum values of G/G_{\max} , respectively, where $G = I/(V_m - E_{rev})$ and G_{\max} is the maximal macroscopic conductance, where I is the measured peak current at each test potential (V_m). All data values are presented as mean \pm s.e.m. n values represent the number of oocytes or number of cells. Statistical significance of the observed effects was assessed using unpaired *t*-tests using GraphPad Prism (v.9.3.1). $P < 0.01$ was considered to be significant, unless otherwise stated.

P values for Fig. 5c are as follows: $P = 0.0007$ ($\text{Ca}_v1.2(\Delta C)$), $P = 0.0321$ ($\text{Ca}_v1.2(\Delta C:3A)-\text{Ca}_v\beta_3$), $P = 0.0799$ ($\text{Ca}_v1.2(\Delta C)-\text{Ca}_v\beta_3(5A)$), $P = 0.0298$ ($\text{Ca}_v1.2(\Delta C)-\text{Ca}_v\beta_3(\Delta 220-240)$), $P = 0.0028$ ($\text{Ca}_v1.2(\Delta C)-\text{Ca}_v\beta_3(5A:\Delta 220-240)$), $P = 0.0019$ ($\text{Ca}_v1.2(\Delta C)-\text{Ca}_v\beta_3(11A)$), $P = 0.0028$ ($\text{Ca}_v1.2(\Delta C:3A)-\text{Ca}_v\beta_3(11A)$), $P < 0.0001$ ($\text{Ca}_v1.2(\Delta C)-\text{Ca}_v\beta_3$ EMC5 knockout), $P = 0.0013$ ($\text{Ca}_v1.2(\Delta C)-\text{Ca}_v\beta_3$ EMC6 knockout) and $P = 0.3513$ ($\text{Ca}_v1.2(\Delta C)-\text{Ca}_v\beta_3(\text{HEK293FT})$).

Stain-free gel image analysis and in-gel digestions for MS analysis

Purified protein samples were diluted in 4× Laemmli Sample Buffer (Bio-Rad) containing 10% β-mercaptoethanol. The samples (1 µg of protein per well) were loaded onto a protein gel (BioRad, 4–15% Criterion TGX Stain-Free Precast Gel). Gels were run at 200 V for 42 min and imaged on a gel imager (BioRad, ChemiDoc MP) using the stain-free gel setting. Gels were stained with colloidal blue stain (Invitrogen) overnight at room temperature with gentle agitation. Excess stain was removed by briefly (3 min) rinsing the gel in de-stain solution (50% water, 40% methanol, 10% acetic acid) followed by three 15 min washes with MilliQ water. Gel lanes were cut into thirds. Each gel slice was subsequently diced into approximately 1 mm cubes. Gel cubes corresponding to a single gel slice were transferred to a 1.5 ml microcentrifuge tube (Protein Lo-Bind, Eppendorf). Ammonium bicarbonate (100 mM; ABC) was added to each tube (75 µl, or enough to completely cover gel cubes), and the samples were incubated for 10 min at room temperature. ABC solution was pipetted away with gel-loading tips (VWR). A total of 100 µl of 100 mM ABC and 10 µl of DTT (50 mM) was added to each sample before incubating at 55 °C (400 rpm, for 30 min). Excess buffer was removed with a gel-loading tip and replaced with 100 µl of 100 mM ABC and 10 µl of 150 mM iodoacetamide. The samples were incubated in the dark for 30 min at room temperature. Buffer was removed, and gel cubes were washed twice with 150 µl of 1:100 mM ABC:acetonitrile on a rotator at room temperature for 10 min. After the last wash, gel cubes were dehydrated with 100 µl of acetonitrile. Excess acetonitrile was removed using a speed-vac for 30 min. A total of 150 µl of 3.3 ng µl⁻¹ trypsin (Promega) in ABC (50 mM) was added to each sample (0.5 µg trypsin per sample) and incubated on a shaker (300 rpm) at 37 °C for 16 h.

After digestion, the samples were acidified and peptides were eluted through the addition of 250 µl of a 66% acetonitrile, 33% ABC (100 mM), 1% formic acid solution. The samples were then centrifuged at 10,000*g* for 2 min, and the resulting supernatants were transferred to new Protein LoBind tubes (Eppendorf). The peptide elution step was repeated and the corresponding supernatants were combined. The samples were then dried using a speed-vac for 2 h.

Crude dried peptides were cleaned using ZipTip C18 columns (Millipore) according to the manufacturer's instructions. In brief, peptides were resuspended in 20 µl of resuspension buffer (5:95 acetonitrile:MilliQ H₂O, 0.1% trifluoroacetic acid) and solubilized in a bath sonicator (VWR, 35 kHz, 10 min). A ZipTip was placed onto a P10 pipettor set to 10 µl, and the C18 column was activated twice with 10 µl of hydration buffer (50:50 acetonitrile:MilliQ H₂O, 0.1% trifluoroacetic acid), followed by a single wash step with 10 µl of wash buffer (0.1% trifluoroacetic acid in water). Peptides were loaded onto the C18 ZipTip column by taking up 10 µl of sample and slowly pipetting up and down 10 times. This loading step was repeated once more before washing twice with 10 µl of wash buffer. Finally, 10 µl of elution buffer (60:40 acetonitrile:MilliQ H₂O, 0.1% trifluoroacetic acid) was taken up into the ZipTip and expelled into a fresh LoBind tube, followed by pipetting up and down 10 times inside the tube. The elution step was repeated once. Eluted peptides were dried using the speed-vac for 20 min and then stored at –20 °C until MS analysis.

Before MS analysis, peptides were resuspended in loading buffer (2% acetonitrile, 0.1% formic acid) and completely solubilized in a bath sonicator (VWR, 35 kHz, 10 min).

MS acquisition and analysis

LC and timsTOF Pro. A nanoElute (Bruker) was attached in line to a timsTOF Pro equipped with a CaptiveSpray Source (Bruker). Chromatography was conducted at 40 °C through a 25 cm reversed-phase C18 column (PepSep) at a constant flow-rate of 0.5 µl min⁻¹. Mobile phase A was 98/2/0.1% liquid chromatography (LC)–MS grade H₂O/acetonitrile/formic acid (v/v/v) and phase B was LC–MS grade acetonitrile with 0.1% formic acid (v/v). During a 108-min method, peptides were separated by a three-step linear gradient (5% to 30% B over 90 min, 30% to 35% B over 10 min, 35% to 95% B over 4 min) followed by a 4-min isocratic flush at 95% before washing and a return to low organic conditions. Experiments were run as data-dependent acquisitions with ion mobility activated in PASEF mode. MS and MS/MS spectra were collected with *m/z* 100 to 1,700 and ions with *z* = +1 were excluded.

Raw data files were searched using PEAKS Online Xpro 1.6 (Bioinformatics Solutions). The precursor mass error tolerance and fragment mass error tolerance were set to 20 PPM and 0.05, respectively. The trypsin digest mode was set to semi-specific and missed cleavages was set to 3. The human Swiss-Prot reviewed (canonical) database (downloaded from UniProt) and the common repository of adventitious proteins (cRAP, downloaded from The Global Proteome Machine Organization) totalling 20,487 entries were used. Carbamidomethylation was selected as a fixed modification. Acetylation (N-term), deamidation (NQ) and oxidation (M) were selected as variable modifications. The maximum number of variable post translational modifications per peptide was 3.

All experiments were repeated in triplicate and the combined datasets were filtered using the following criteria: (1) all proteins from the common contaminants search database and all keratins were removed; (2) required a protein to be found in all three replicates of at least one condition; (3) at least 20% coverage; (4) at least 4 peptides and 4 unique peptides; (5) median area of at least 25,000 across all 3 replicates in the $\text{Ca}_v1.2(\Delta C)-\text{Ca}_v\beta_3$ sample (denoted as Alpha+Beta in Supplementary Table 1).

Raw data files and searched datasets are available at the Mass Spectrometry Interactive Virtual Environment, a member of the Proteome Xchange consortium (<https://massive.ucsd.edu/>) under the identifier MSV000090434. The filtered dataset is also available in Supplementary Table 1.

Sample preparation and cryo-EM data acquisition

For cryo-EM, 3.5 µl of 1.7 mg ml⁻¹ $\text{Ca}_v1.2(\Delta C)-\text{Ca}_v\beta_3$ sample or 2.7 mg ml⁻¹ $\text{Ca}_v1.2(\Delta C)-\text{Ca}_v\beta_3-\text{Ca}_v\alpha_2\delta$ sample was applied to Quantifoil R1.2/1.3 300 mesh Au holey-carbon grids, blotted for 4–6 s at 4 °C and 100%

Article

humidity using a FEI Vitrobot Mark IV (Thermo Fisher Scientific) and plunge-frozen in liquid ethane. Cryo-EM grids were screened on the FEI Talos Arctica cryo-TEM system (Thermo Fisher Scientific) (at University of California, San Francisco (UCSF) EM Facility and SLAC National Accelerator Laboratory) operated at 200 kV and equipped with a K3 direct detector camera (Gatan), and then imaged on a 300 kV FEI Titan Krios microscope (Thermo Fisher Scientific) with a K3 direct detector camera (Gatan) (UCSF). Cryo-EM datasets were collected in super-resolution counting mode at a nominal magnification of $\times 105,000$ with a super-resolution pixel size of 0.4233 Å (physical pixel size of 0.8466 Å) using SerialEM⁸³. Images were recorded with a 2.024 s exposure over 81 frames with a dose rate of 0.57 e⁻ Å⁻² per frame. The defocus range was set from -0.9 μm to -1.7 μm.

Image processing and 3D reconstruction

A total of 14,341 and 13,704 movie stacks were collected for the Ca_v1.2(ΔC)-Ca_vβ₃ and Ca_v1.2(ΔC)-Ca_vβ₃-Ca_vα₂δ samples, respectively. Initial image processing was performed in cryoSPARC-3.2 (ref. 84). Raw movies were motion-corrected by a factor of two (final pixel size of 0.8466 Å) using the patch motion correction program. Contrast transfer function parameters of the resulting micrographs were estimated using the patch CTF program in cryoSPARC-3.2. Particles were picked by blob picking, extracted using a box size of 440 Å. Particles were subsequently template picked with 2D class averages low-pass filtered to 20 Å and extracted using 440 Å box size. After several rounds of clean-up using reference-free 2D classification, an ab initio model was generated and heterogenous refinement was then performed without imposing any symmetry. Particles with reasonable 3D reconstructions (as judged by the Fourier shell correlation curve shapes) were processed for non-uniform refinement to archive 3D reconstructions with the highest resolution.

To improve the features of each 3D reconstruction, multibody refinement was performed in RELION-3.1 (ref. 85). For Ca_v1.2-Ca_vβ₃, 239,729 refined particles were exported from cryoSPARC-3.2 to RELION-3.1 using the csparc2star.py (UCSF pyem v.0.5) suite of conversion scripts (<https://doi.org/10.5281/zenodo.3576630>). After 3D refinement in RELION-3.1 using the refined map from cryoSPARC-3.2 and the exported particles, an overall 3.4 Å EM density map was obtained (EMC:Ca_v1.2-Ca_vβ₃ (ECAB) map 1) (processing flow charts are shown in Extended Data Fig. 1i). To improve the map features of the flexible regions, multibody refinement was performed in RELION-3.1 using two bodies: (1) body I containing the luminal domain (that is, EMC1, EMC4, EMC7 and EMC10) and the transmembrane region (Ca_v1.2, EMC1 TM1, EMC3 TM1-3, EMC5 TM1-2 and EMC6) of ECAB map 1; and (2) body II containing the cytoplasmic domain (Ca_vβ₃, EMC2, EMC8, and the cytoplasmic segments of EMC3 and EMC5) and an overlapping portion of the transmembrane region. The phenix.combine_focused_maps program was used to combine the two segments with improved features from multibody refinement⁸⁶. A similar strategy was applied to 269,950 particles of ECAB map 2 to obtain a 3.6 Å consensus map, followed by feature improvement using multibody refinement in RELION-3.1. ECAB map 1 and ECAB map 2 (cross correlation = 0.9836) were merged using Phenix to obtain ECAB map 3 with the best features⁸⁶. The pool of 269,802 particles of Ca_v1.2-Ca_vβ₃-Ca_vα₂δ (CABAD) map 1 was exported from cryoSPARC using the strategy as described above and processed for refinement in RELION-3.1, yielding a 3.3 Å consensus map. This map and particle set was further used to perform a two-body multibody refinement according to the procedure described above to obtain CABAD map 2.

Model building and refinement

ECAB map 3 and CABAD map 2 were used to build the model for the EMC-Ca_v1.2(ΔC)-Ca_vβ₃ complex and the Ca_v1.2(ΔC)-Ca_vβ₃-Ca_vα₂δ-1 complex, respectively. For the EMC-Ca_v1.2(ΔC)-Ca_vβ₃ complex, a preliminary model was built using the previously reported apo-EMC structure (Protein Data Bank (PDB): 6WW7)²⁹ and the Ca_vβ₃ subunit in

the Ca_v2.2 structure (PDB: 7MIY)⁴⁵. For the Ca_v1.2(ΔC)-Ca_vβ₃-Ca_vα₂δ-1 complex, the Ca_v2.2 structure (PDB: 7MIY)⁴⁵ was used as starting model. Phyre2 server⁸⁷ was used to predict ten models of Ca_v1.2 using amino acid sequences (UniProt: Q13936-20) and, among them, the best model was selected by comparing them with the density map. The phenix.dock_in_map program was used to dock the models in respective maps⁸⁶. As the density for Ca_vβ₃ in the Ca_v1.2(ΔC)-Ca_vβ₃-Ca_vα₂δ-1 complex was weaker than for other parts of the channel, we rendered the Ca_vβ region of the Ca_v1.2(ΔC)-Ca_vβ₃-Ca_vα₂δ-1 complex at a threshold of 2.25 (>5 was used for the rest of map) and placed Ca_vβ₃ from the de novo modelled EMC-Ca_v1.2(ΔC)-Ca_vβ₃ structure in the density, followed by rigid-body refinement of the Ca_v1.2(ΔC)-Ca_vβ₃-Ca_vα₂δ-1 complex. The docked model and maps were further manually checked and fitted in COOT⁸⁸. Iterative structure refinement and model building were performed using the phenix.real_space_refine program⁸⁶. The local resolution range for Ca_v1.2 was 2.0–4.8 Å (Supplementary Fig. 3e), which allowed model building by putting more emphasis on helix topology and large aromatic side-chain densities. However, model building was strictly performed on the basis of the available electron density. Restraint files necessary for refinement were generated using phenix.elbow^{86,89}. Final statistics of 3D reconstruction and model refinement are provided in Extended Data Table 1. The per-residue B-factors, after final refinement against the overall map, were rendered on the refined model and are presented in Supplementary Fig. 3c–f. The final models were evaluated using MolProbity⁹⁰. All figures and videos were generated using ChimeraX⁹¹ and the Pymol package (<http://www.pymol.org/pymol>). Close-contact interaction analysis was performed using LIGPLOT and DIMPLOT^{92,93}.

Reporting summary

Further information on research design is available in the Nature Portfolio Reporting Summary linked to this article.

Data availability

Coordinates and maps of the EMC-Ca_v1.2(ΔC)-Ca_vβ₃ complex (PDB: 8EOI; Electron Microscopy Data Bank (EMDB): EMD-28376, EMD-28578, EMD-28579, EMD-40559, EMD-40560) and Ca_v1.2(ΔC)-Ca_vβ₃-Ca_vα₂δ-1 complex (PDB: 8EOF; EMDB: EMD-28375, EMD-28561, EMD-28564, EMD-40561) have been deposited at the PDB and EMDB. MS data have been deposited at the Mass Spectrometry Interactive Virtual Environment (<https://massive.ucsd.edu/>) under identifier MSV000090434. Source data are provided with this paper.

74. Schmidt, T. G. & Skerra, A. The Strep-tag system for one-step purification and high-affinity detection or capturing of proteins. *Nat. Protoc.* **2**, 1528–1535 (2007).
75. Liao, M., Cao, E., Julius, D. & Cheng, Y. Structure of the TRPV1 ion channel determined by electron cryo-microscopy. *Nature* **504**, 107–112 (2013).
76. Elelgeert, J. et al. Lentiviral transduction of mammalian cells for fast, scalable and high-level production of soluble and membrane proteins. *Nat. Protoc.* **13**, 2991–3017 (2018).
77. Goehring, A. et al. Screening and large-scale expression of membrane proteins in mammalian cells for structural studies. *Nat. Protoc.* **9**, 2574–2585 (2014).
78. Lee, H., Lolicato, M., Arrigoni, C. & Minor, D. L. Jr. Production of K2P2.1 (TREK-1) for structural studies. *Methods Enzymol.* **653**, 151–188 (2021).
79. Shaya, D. et al. Voltage-gated sodium channel (Nav) protein dissection creates a set of functional pore-only proteins. *Proc. Natl Acad. Sci. USA* **108**, 12313–12318 (2011).
80. Abderemane-Ali, F., Findeisen, F., Rossen, N. & Minor Jr, D. L. A selectivity filter gate controls voltage-gated calcium channel calcium-dependent inactivation. *Neuron* **101**, 1134–1149 (2019).
81. Findeisen, F. & Minor Jr, D. L. Disruption of the IS6-AID linker affects voltage-gated calcium channel inactivation and facilitation. *J. Gen. Physiol.* **133**, 327–343 (2009).
82. Hamill, O. P., Marty, A., Neher, E., Sakmann, B. & Sigworth, F. J. Improved patch-clamp techniques for high-resolution current recording from cells and cell-free membrane patches. *Pflügers Arch.* **391**, 85–100 (1981).
83. Mastronarde, D. N. Automated electron microscope tomography using robust prediction of specimen movements. *J. Struct. Biol.* **152**, 36–51 (2005).
84. Punjani, A., Rubinstein, J. L., Fleet, D. J. & Brubaker, M. A. cryoSPARC: algorithms for rapid unsupervised cryo-EM structure determination. *Nat. Methods* **14**, 290–296 (2017).
85. Zivanov, J. et al. New tools for automated high-resolution cryo-EM structure determination in RELION-3. *eLife* **7**, e42166 (2018).
86. Liebschner, D. et al. Macromolecular structure determination using X-rays, neutrons and electrons: recent developments in Phenix. *Acta Crystallogr. D* **75**, 861–877 (2019).

87. Kelley, L. A., Mezulis, S., Yates, C. M., Wass, M. N. & Sternberg, M. J. The Phyre2 web portal for protein modeling, prediction and analysis. *Nat. Protoc.* **10**, 845–858 (2015).
88. Emsley, P., Lohkamp, B., Scott, W. G. & Cowtan, K. Features and development of Coot. *Acta Crystallogr. D* **66**, 486–501 (2010).
89. Moriarty, N. W., Grosse-Kunstleve, R. W. & Adams, P. D. Electronic Ligand Builder and Optimization Workbench (eLBOW): a tool for ligand coordinate and restraint generation. *Acta Crystallogr. D* **65**, 1074–1080 (2009).
90. Williams, C. J. et al. MolProbit: more and better reference data for improved all-atom structure validation. *Protein Sci.* **27**, 293–315 (2018).
91. Pettersen, E. F. et al. UCSF ChimeraX: structure visualization for researchers, educators, and developers. *Protein Sci.* **30**, 70–82 (2021).
92. Wallace, A. C., Laskowski, R. A. & Thornton, J. M. LIGPLOT: a program to generate schematic diagrams of protein-ligand interactions. *Protein Eng.* **8**, 127–134 (1995).
93. Laskowski, R. A. & Swindells, M. B. LigPlot+: multiple ligand-protein interaction diagrams for drug discovery. *J. Chem. Inf. Model.* **51**, 2778–2786 (2011).

Acknowledgements We thank T.-J. Yen, D. Bulkley, Y. Liu and H. Khant for technical help; T. Pleiner and R. Vorhees for the HEK293FT cells and *EMC5*-knockout and *EMC6*-knockout lines; and K. Brejc, H. M. Colecraft, D. Julius and G. Thiel for comments on the manuscript. This work was supported by grants NIH R01 HL080050 and NIH R01 DC007664 to D.L.M.; the Beckman Foundation to B.W.Z.; the National Science Foundation GRFP DGE-2034836 to J.L.M.; and an American Heart Association postdoctoral fellowship to F.A.-A. B.W.Z. is a Beckman Young

Investigator. Some of this work was performed at the Stanford-SLAC Cryo-EM Center (S^2C^2), which is supported by the National Institutes of Health Common Fund Transformative High-Resolution Cryo-Electron Microscopy program (U24 GM129541). The content is solely the responsibility of the authors and does not necessarily represent the official views of the National Institutes of Health.

Author contributions Z.C. and D.L.M. conceived the study and designed the experiments. Z.C. and S.N. expressed and characterized the samples. Z.C., A.M. and F.A.-A. collected and analysed cryo-EM data. Z.C. and A.M. built and refined the atomic models. Z.C. collected and analysed the two-electrode voltage clamp data. F.A.-A. and S.J. collected and analysed the whole-cell electrophysiology data. J.L.M. and B.W.Z. collected and analysed the MS data. B.W.Z. and D.L.M. analysed data and provided guidance and support. Z.C., A.M., F.A.-A., J.L.M., B.W.Z. and D.L.M. wrote the paper.

Competing interests The authors declare no competing interests.

Additional information

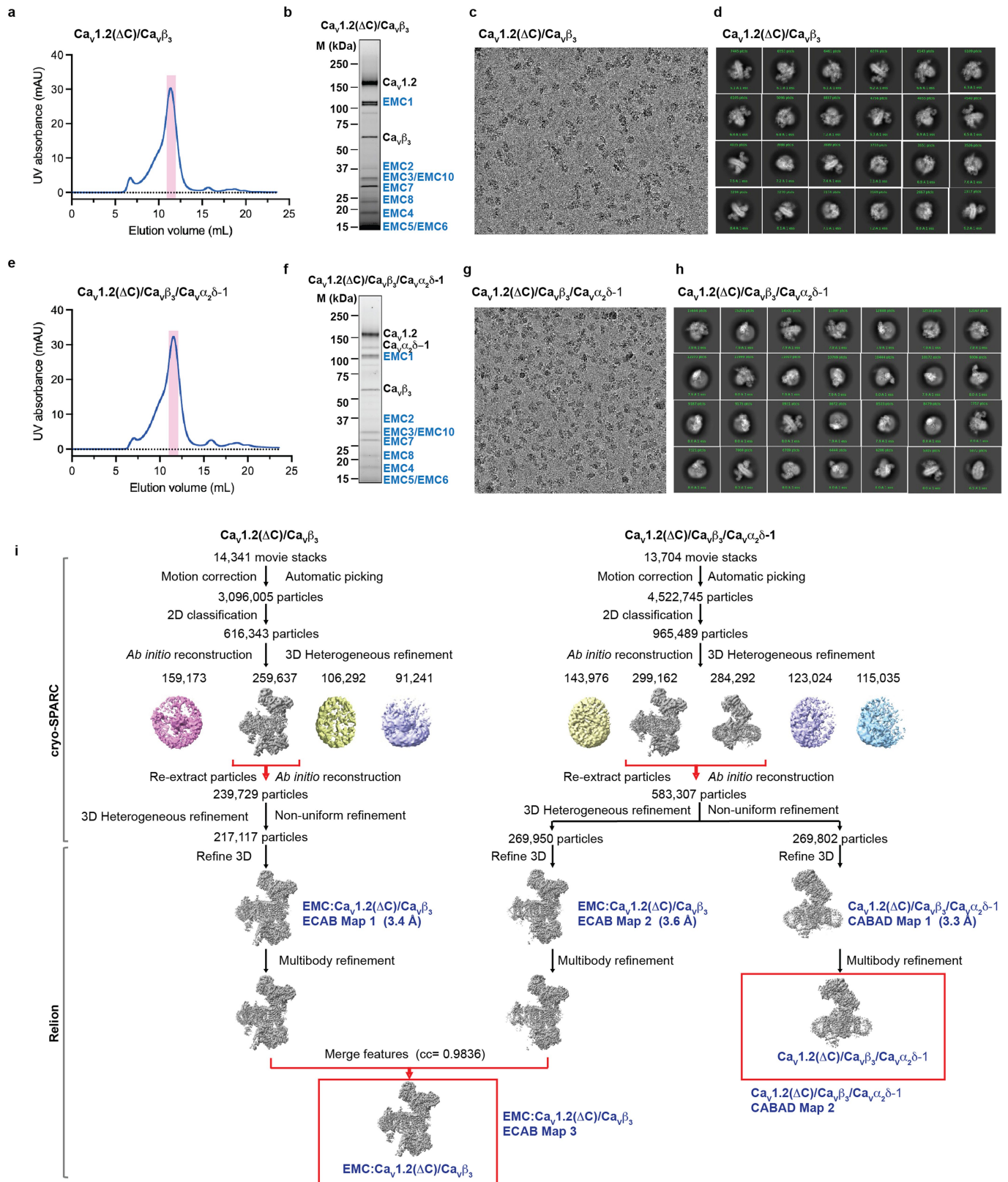
Supplementary information The online version contains supplementary material available at <https://doi.org/10.1038/s41586-023-06175-5>.

Correspondence and requests for materials should be addressed to Daniel L. Minor.

Peer review information *Nature* thanks the anonymous reviewers for their contribution to the peer review of this work. Peer reviewer reports are available.

Reprints and permissions information is available at <http://www.nature.com/reprints>.

Article



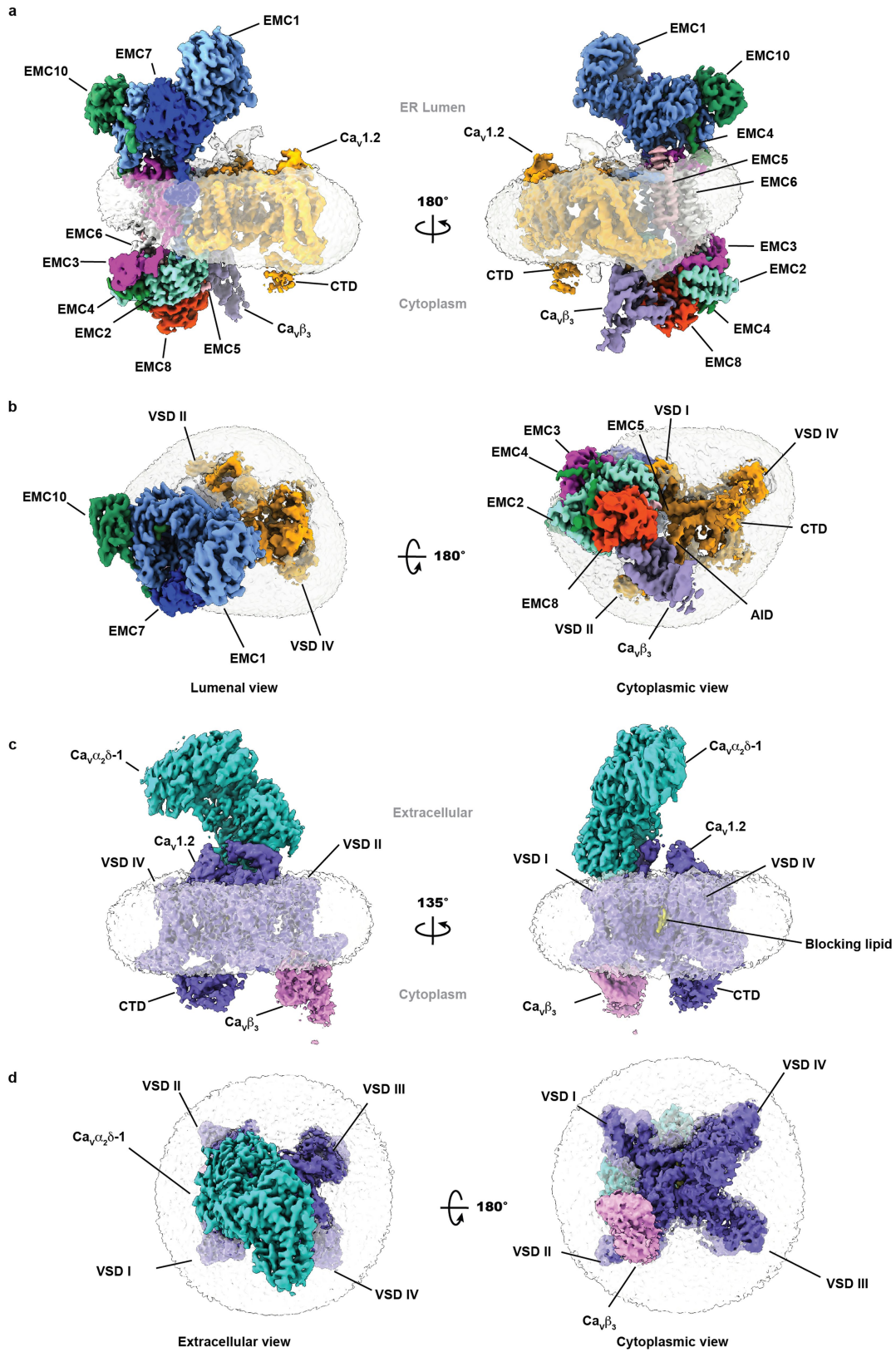
Extended Data Fig. 1 | See next page for caption.

Extended Data Fig. 1 | EMC:Ca_v1.2(ΔC)/Ca_vβ₃ and Ca_v1.2(ΔC)/Ca_vβ₃/Ca_vα₂δ-1

Cryo-EM analysis. **a-d**, Exemplars of purified Ca_v1.2(ΔC)/Ca_vβ₃; **a**, SEC (Superose 6 Increase 10/300 GL). **b**, peak fraction SDS-PAGE. **c**, electron micrograph (~105,000x magnification), and **d**, 2D class averages. **e-h** Exemplars of purified Ca_v1.2(ΔC)/Ca_vβ₃/Ca_vα₂δ-1; **e**, SEC (Superose 6 Increase 10/300 GL). **f**, peak fraction SDS-PAGE. Magenta bars in 'a' and 'e' mark peak fraction. **g**, electron micrographs (~105,000x magnification), and **h**, 2D class averages. **i**, Workflow for electron microscopy data processing for the Ca_v1.2(ΔC)/Ca_vβ₃ and Ca_v1.2(ΔC)/Ca_vβ₃/Ca_vα₂δ-1 samples. Initial cryoSPARC-3.2 *Ab initio* reconstruction identified a population of particles containing the EMC:Ca_v1.2(ΔC)/Ca_vβ₃ complex in the Ca_v1.2(ΔC)/Ca_vβ₃ sample and populations of particles containing either the EMC:Ca_v1.2(ΔC)/Ca_vβ₃ complex or Ca_v1.2(ΔC)/Ca_vβ₃/Ca_vα₂δ-1 complex in the

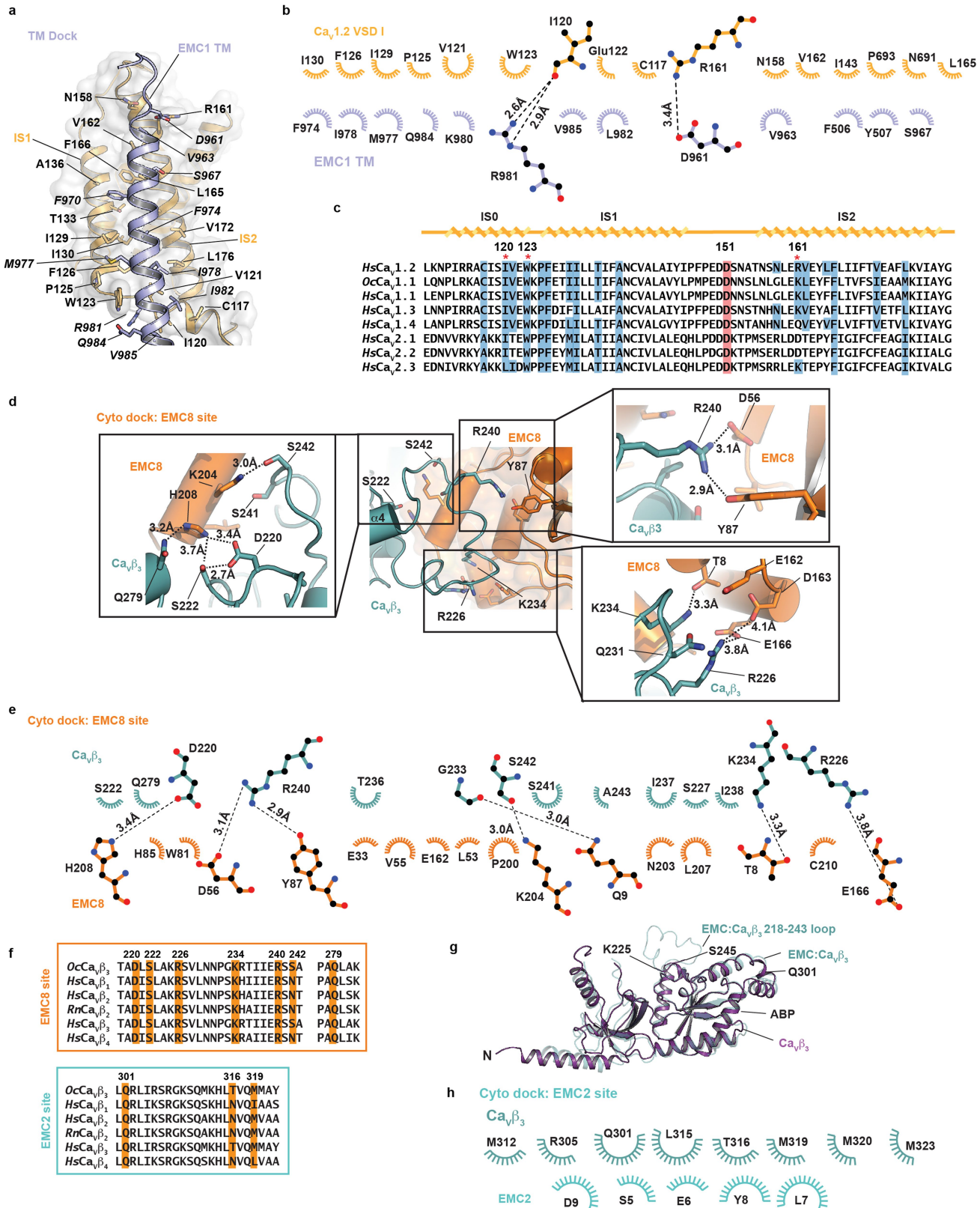
Ca_v1.2(ΔC)/Ca_vβ₃/Ca_vα₂δ-1 sample. Red arrows indicate the three classes that were re-extracted, subjected to multiple rounds of 3D heterogeneous classification, and exported from cryoSPARC-3.2 for further 3D refinement in RELION-3.1. This resulted in two maps for the EMC:Ca_v1.2(ΔC)/Ca_vβ₃ complex (ECAB Maps 1 and 2) and one for the Ca_v1.2(ΔC)/Ca_vβ₃/Ca_vα₂δ-1 complex (CABAD Map 1). Multibody refinement was performed in RELION-3.1 to improve the features of flexible regions of the three maps. This resulted in the final map for the Ca_v1.2(ΔC)/Ca_vβ₃/Ca_vα₂δ-1 complex (CABAD Map 2). ECAB Maps 1-2 with improved flexible features were merged (cross correlation = 0.9836) to obtain the final map for the EMC:Ca_v1.2(ΔC)/Ca_vβ₃ complex (ECAB Map 3). Red boxes indicate the final maps used for model building. For 'b-c', N = 3. For 'f-g', N = 2.

Article



Extended Data Fig. 2 | Cryo-EM maps of EMC:Ca_v1.2(ΔC)/Ca_vβ₃ and Ca_v1.2(ΔC)/Ca_vβ₃/Ca_vα₂δ-1 complexes. EMC:Ca_v1.2(ΔC)/Ca_vβ₃ complex **a**, side views and **b**, luminal (left) and cytoplasmic (right) views. Subunits are coloured as: EMC1 (light blue), EMC2 (aqua), EMC3 (light magenta), EMC4 (Forest), EMC5 (light pink), EMC6 (white), EMC7 (marine), EMC8 (orange), EMC10 (smudge),

Ca_v1.2 (bright orange), and Ca_vβ₃ (lavender). Ca_v1.2(ΔC)/Ca_vβ₃/Ca_vα₂δ-1 **c**, side views and **d**, extracellular (left) and cytoplasmic (right) views. Subunits are coloured as: Ca_v1.2 (slate), Ca_vβ₃ (violet), and Ca_vα₂δ-1 (greencyan). Detergent micelle is clear.

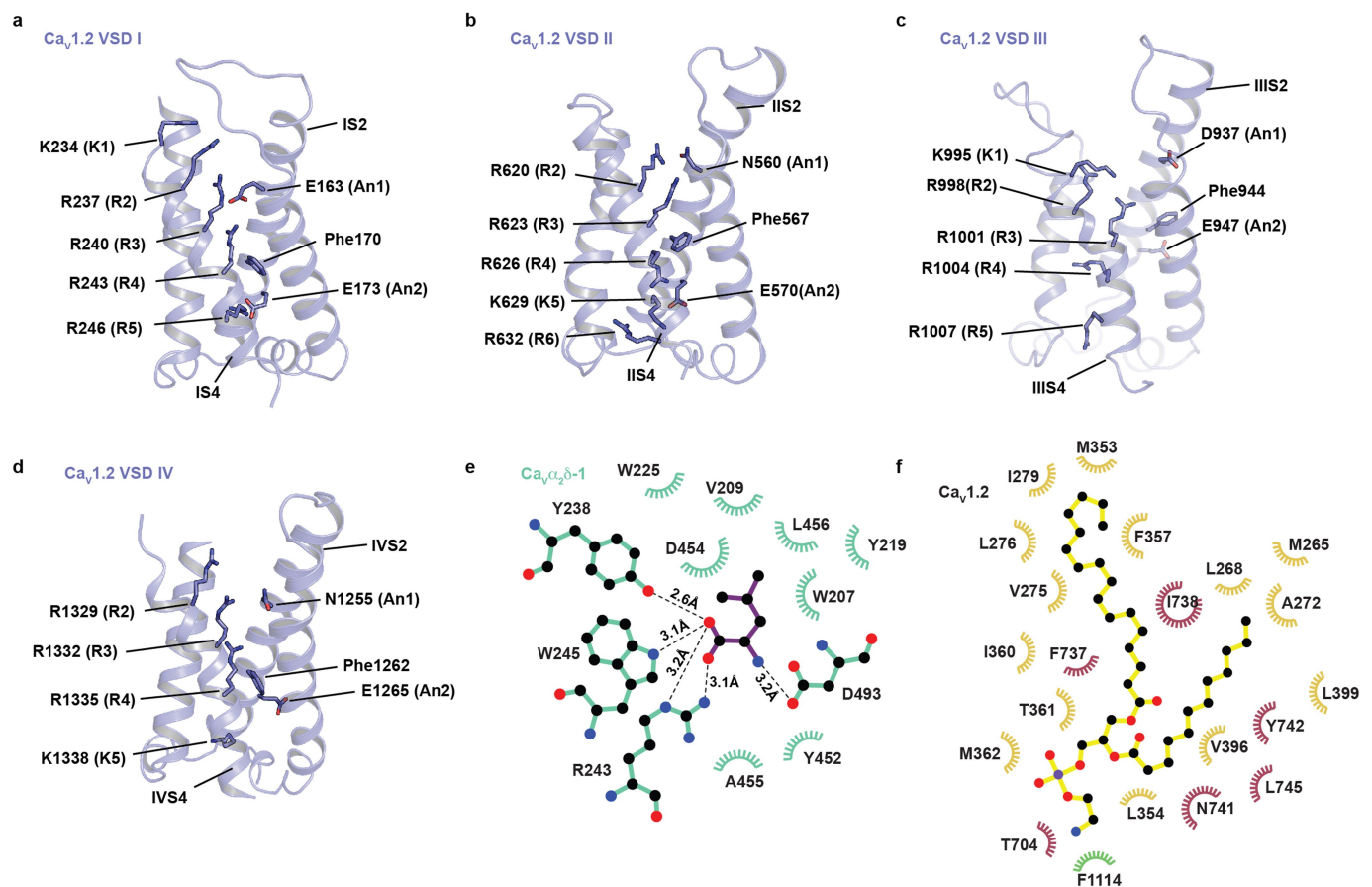


Extended Data Fig. 3 | See next page for caption.

Article

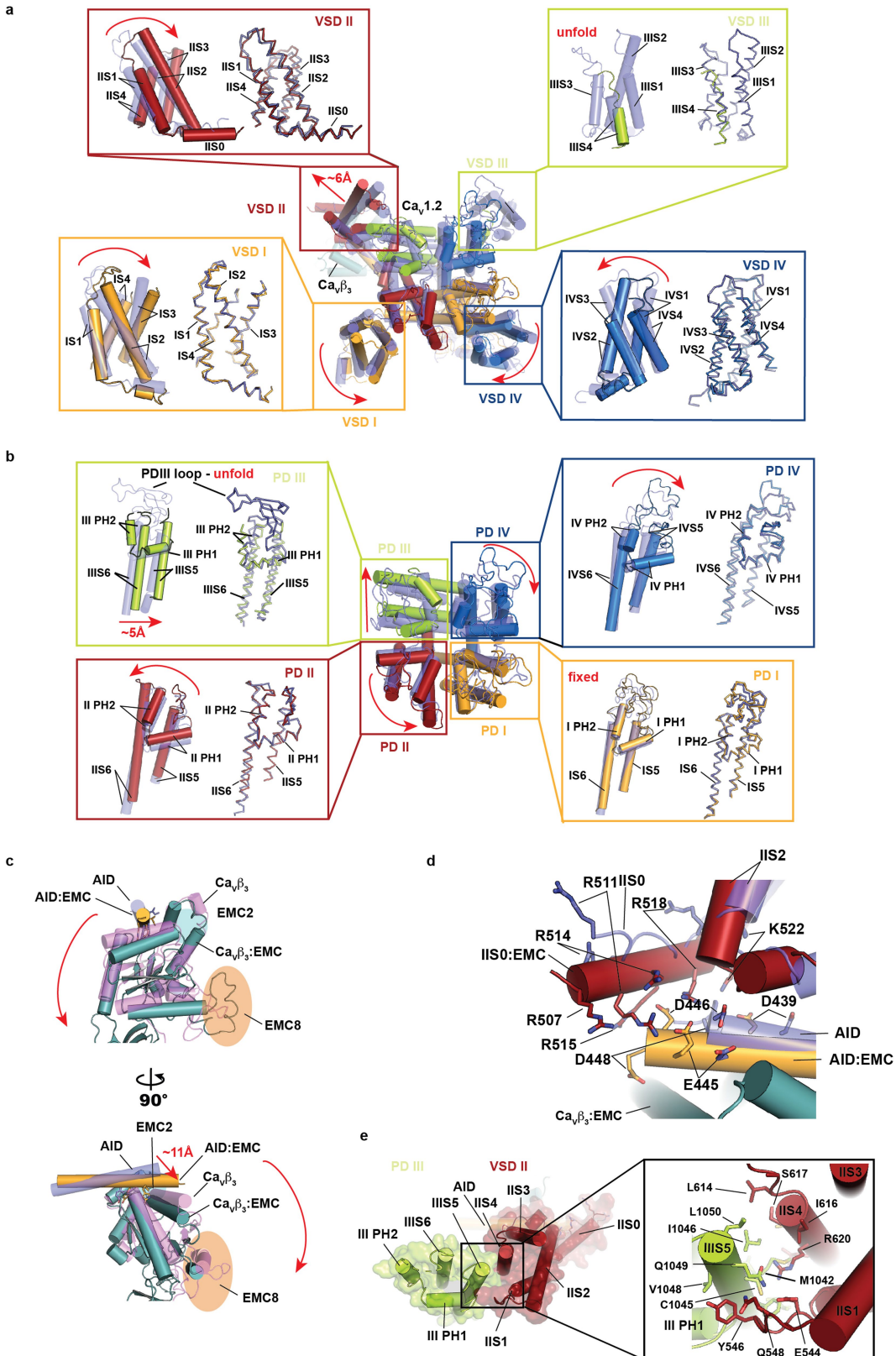
Extended Data Fig. 3 | EMC:Ca_v1.2(ΔC)/Ca_vβ₃ binding sites. **a**, View of the TM dock interaction. EMC1 TM1 (slate) and Ca_v1.2 VSD I (yellow orange) interface. Interface buries 1051 Å². Select elements and residues are indicated. EMC1 residues are in italics. **b**, LigPLOT⁹² diagram of EMC1TM:Ca_v1.2 VSD I interactions showing ionic interactions (dashed lines) and van der Waals contacts ≤ 5 Å. **c**, Sequence comparison of the indicated VSDI sequences for human Ca_v1.2 (*HsCa*_v1.2 (109–182)) (Uniprot Q13936-20) with rabbit Ca_v1.1 (*OcCa*_v1.1 (36–109)) (NCBI: NP_001095190.1), and human L-type (*HsCa*_v1.1 (36–109), *HsCa*_v1.3 (111–184), and *HsCa*_v1.4 (77–150)) (NCBI: NP_000060.2, NP_000711.1, and NP_005174.2) and non-L-Type (*HsCa*_v2.1 (83–156), *HsCa*_v2.2 (80–153), and *HsCa*_v2.3 (74–147)) (NCBI: NP_000059.3, NP_000709.1, and NP_001192222.1) channels. Red asterisks indicate residues involved in the cation-π pocket (120 and 123) and salt bridge (161). Red band highlights the residue that coordinates the Ca²⁺ ion in the Ca_vα₂δ VWA domain. **d**, Ca_vβ₃:EMC8 interaction. Callouts show the details of the indicated parts of the Ca_vβ₃ NK loop interaction

with EMC8. **e**, LigPLOT⁹² diagram of Ca_vβ₃:EMC8 interactions showing ionic interactions (dashed lines) and van der Waals contacts ≤ 5 Å. Ca_vβ:EMC8 hydrogen bond and salt bridge pairs are: Asp220:His208, Ser222:His208, Arg226:Glu166, Lys234:Thr8, Arg240:Asp56/Tyr87, Ser242:Lys204, and Gln279:His208. **f**, Sequence conservation for the indicated Ca_vβ elements from the EMC8 (top) and EMC2 (bottom) interaction sites. *OcCa*_vβ₃ (Uniprot P54286; 218–243, 277–282; 300–322); *HsCa*_vβ₁ (Uniprot Q02641.3; 270–295, 329–334; 352–374); *HsCa*_vβ₂ (Uniprot Q08289; 322–347, 381–386; 404–426); *RnCa*_vβ₂ (Uniprot Q8VGC3; 318–343, 377–382; 400–422); *HsCa*_vβ₃ (Uniprot P54284; 218–243, 277–282; 300–322); *HsCa*_vβ₄ (Uniprot O00305; 260–285, 319–324; 342–364). **g**, Superposition of rat Ca_vβ₃ alone (violet, PDB:1VYU, chain B³⁹) and Ca_vβ₃ from the EMC complex. Boundaries of the disordered part of the T218–A243 loop in Ca_vβ₃, and Q301, and ABP, are indicated, (RMSD_{Ca} = 1.39 Å). **h**, LigPLOT⁹² diagram of Ca_vβ₃:EMC2 interactions showing van der Waals contacts ≤ 5 Å.



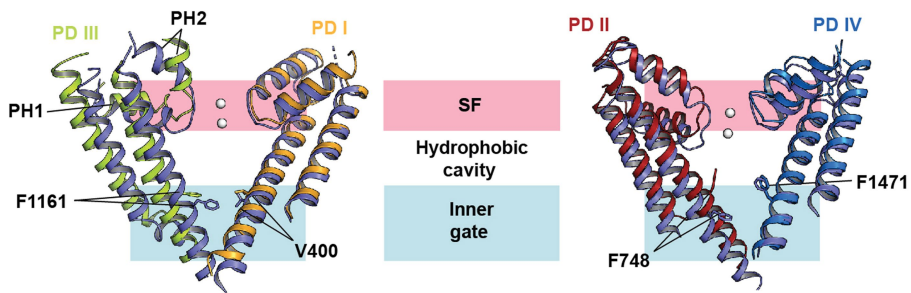
Extended Data Fig. 4 | *Ca_v1.2* structural details. **a–d**, Structures of the indicated VSDs from the *Ca_v1.2*(ΔC)/*Ca_vβ₂*/*Ca_vα₂δ-1* complex. Gating charge residues, anionic counter charges (An1 and An2) and aromatic site of the charge transfer centre^{43,45,55} are shown. **e**, LigPLOT⁹² diagram of the *Ca_vα₂δ-1*-leucine

binding site showing hydrogen bonds and ionic interactions (dashed lines) and van der Waals contacts $\leq 5\text{ Å}$. **f**, LigPLOT⁹² diagram of blocking lipid: *Ca_v1.2* showing van der Waals contacts $\leq 5\text{ Å}$. Domain I (yellow orange), Domain II (dark red), and Domain III (green) residues are indicated.



Extended Data Fig. 5 | Conformational changes between EMC-bound and $\text{Ca}_V\alpha_2\delta$ -bound $\text{Ca}_V1.2(\Delta C)/\text{Ca}_V\beta_3$. Superposition of $\text{Ca}_V1.2$ from the EMC: $\text{Ca}_V1.2(\Delta C)/\text{Ca}_V\beta_3$ and $\text{Ca}_V1.2(\Delta C)/\text{Ca}_V\beta_3/\text{Ca}_V\alpha_2\delta$ complexes showing **a**, VSD conformational changes. **b**, PD conformational changes showing the superposition from 'a'. Insets show each PD. Elements $\text{Ca}_V1.2$ from the EMC complex are: VSD I/PD I (yellow orange), VSD II/PD II (firebrick), VSD III/PD III (lime), VSD IV/PD IV (marine). $\text{Ca}_V1.2$ (slate) and $\text{Ca}_V\beta_3$ (violet) from $\text{Ca}_V1.2(\Delta C)/\text{Ca}_V\beta_3/\text{Ca}_V\alpha_2\delta$ and $\text{Ca}_V\beta_3$ from the EMC (light teal) are semi-transparent.

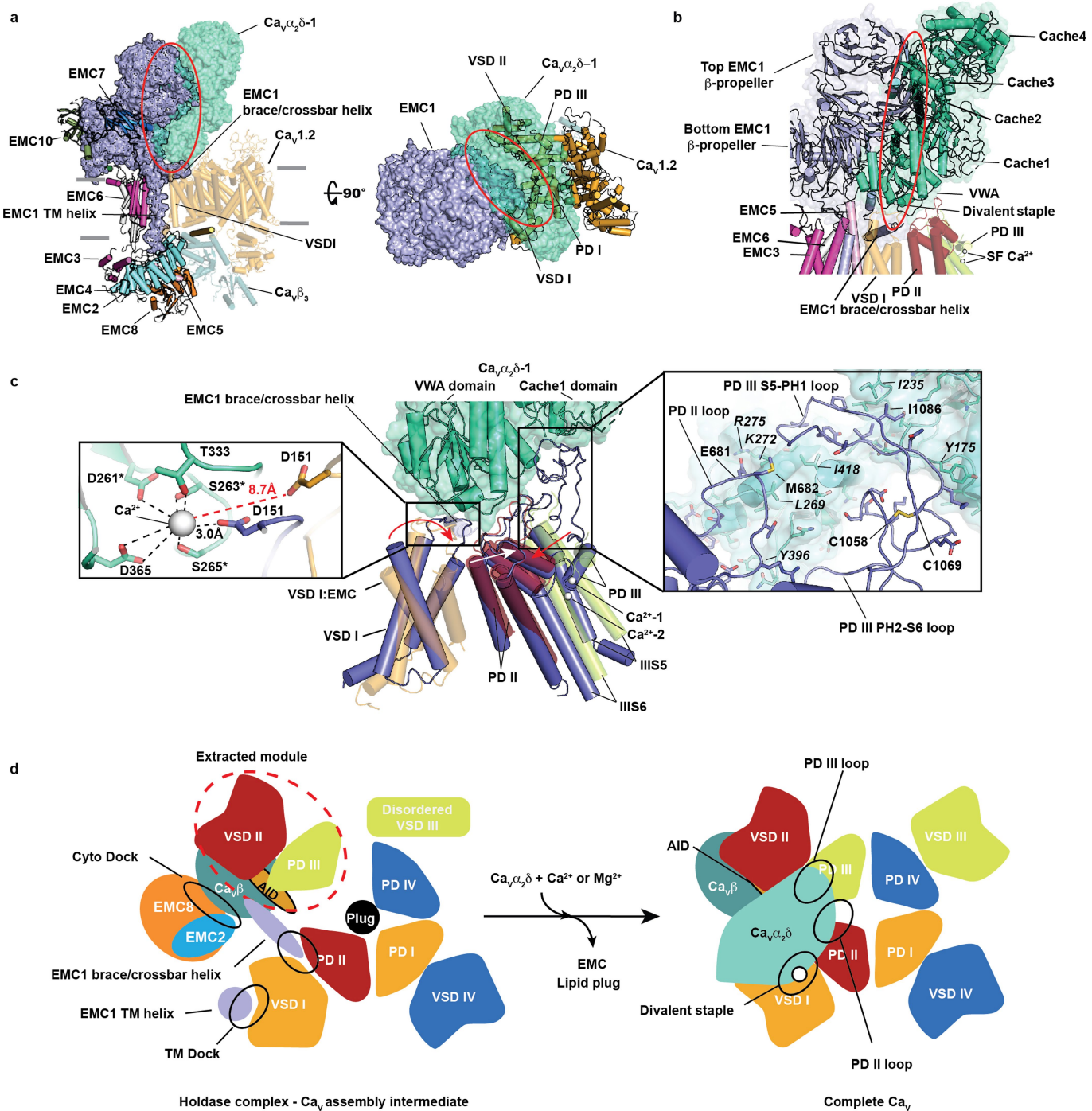
c, Superposition of $\text{Ca}_V\beta_3$ and the $\text{Ca}_V1.2$ AID helix from the EMC: $\text{Ca}_V1.2(\Delta C)/\text{Ca}_V\beta_3$ and $\text{Ca}_V1.2(\Delta C)/\text{Ca}_V\beta_3/\text{Ca}_V\alpha_2\delta$ complexes. Location of EMC8 is indicated by the orange oval. Red arrows in 'a'-c' indicate conformational changes between $\text{Ca}_V1.2(\Delta C)/\text{Ca}_V\beta_3/\text{Ca}_V\alpha_2\delta$ and EMC: $\text{Ca}_V1.2(\Delta C)/\text{Ca}_V\beta_3$. **d**, Comparison of IIS0 and surrounding regions in the EMC complex (VSDII, firebrick; AID (yellow orange), and $\text{Ca}_V\beta_3$ (light teal)) their corresponding elements in $\text{Ca}_V1.2(\Delta C)/\text{Ca}_V\beta_3/\text{Ca}_V\alpha_2\delta$ (slate) and $\text{Ca}_V\beta_3$ (violet). **e**, Interactions between VSD II:PD III in the $\text{Ca}_V\beta_3$:AID:VSD II:PD III subcomplex from the EMC: $\text{Ca}_V1.2(\Delta C)/\text{Ca}_V\beta_3$ structure.



Extended Data Fig. 6 | $\text{Ca}_v1.2$ pore domain superposition for EMC-bound and $\text{Ca}_v\alpha_2\delta$ -bound $\text{Ca}_v1.2(\Delta C)/\text{Ca}_v\beta_3$. Pore domains from the EMC-bound complex are: PD I (yellow orange), PD II (firebrick), PD III (lime), and PD IV

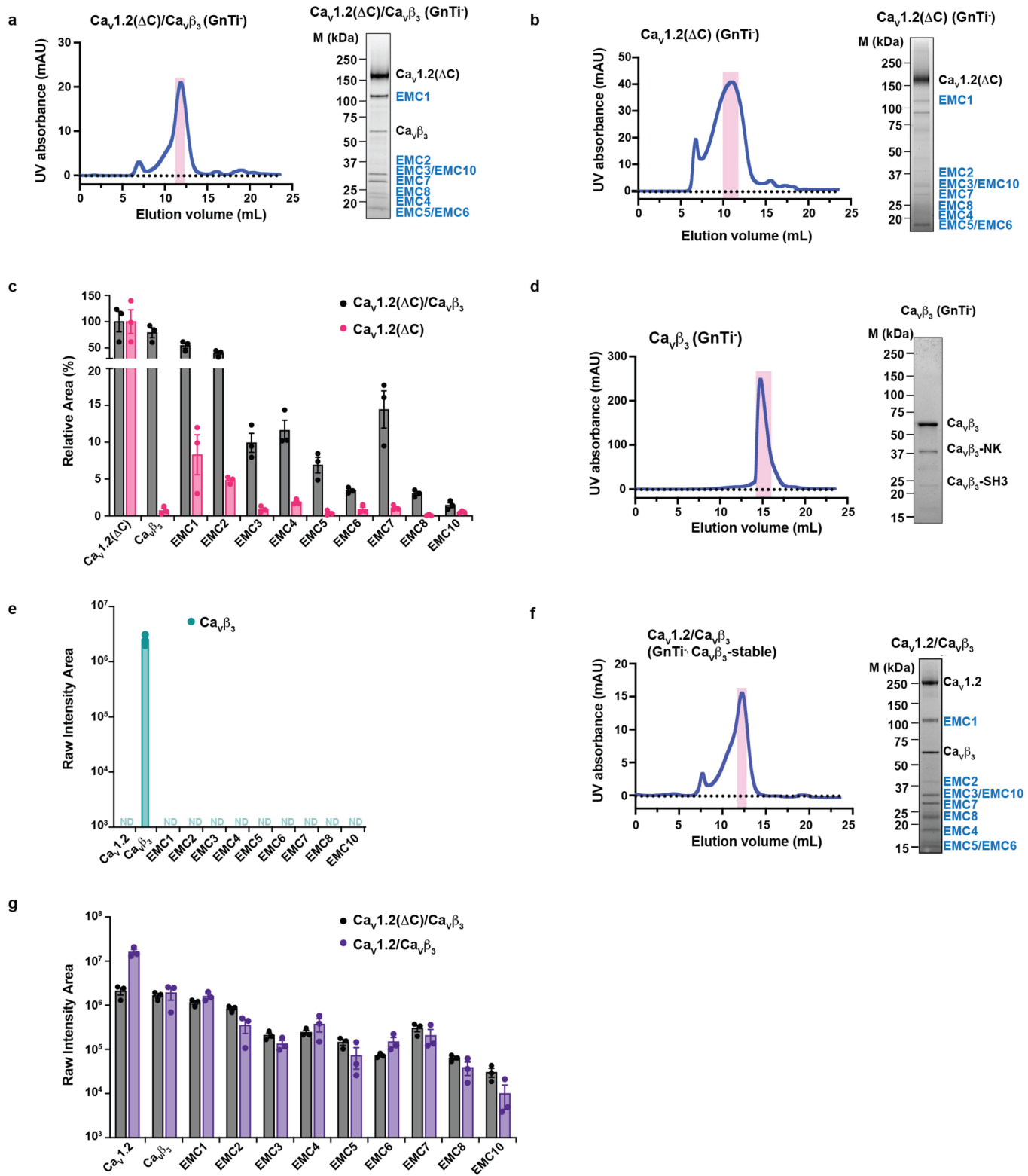
(marine). Pore domains from $\text{Ca}_v1.2(\Delta C)/\text{Ca}_v\beta_3/\text{Ca}_v\alpha_2\delta-1$ are slate. Calcium ions are from $\text{Ca}_v1.2(\Delta C)/\text{Ca}_v\beta_3/\text{Ca}_v\alpha_2\delta-1$. Selectivity filter (SF), hydrophobic cavity, and inner gate regions and select residues are indicated.

Article



Extended Data Fig. 7 | Mutually exclusive interactions of the EMC holdase and $\text{Ca}_v\alpha_2\delta$ with the core $\text{Ca}_v1.2/\text{Ca}_v\beta_3$ complex and ordering of the $\text{Ca}_v1.2$ pore and VSDs by $\text{Ca}_v\alpha_2\delta$. **a**, Superposition of $\text{Ca}_v\alpha_2\delta-1$ (semi-transparent, aquamarine) from the $\text{Ca}_v1.2(\Delta C)/\text{Ca}_v\beta_3/\text{Ca}_v\alpha_2\delta-1$ structure with the EMC: $\text{Ca}_v1.2/\text{Ca}_v\beta_3$ complex. EMC1 surface is shown. Red oval highlights clash regions. Colours of the EMC: $\text{Ca}_v1.2/\text{Ca}_v\beta_3$ complex are as in Fig. 1a. Grey bars denote the membrane. **b**, Close up view of clash between EMC1 (light blue) and $\text{Ca}_v\alpha_2\delta-1$ (aquamarine). EMC1, EMC3 (magenta), EMC5 (pink), EMC6 (white), VSD1 (yellow orange), PD II (firebrick), and PD III (lime) from the EMC: $\text{Ca}_v1.2/\text{Ca}_v\beta_3$ complex are shown. Red oval highlights clash regions. $\text{Ca}_v\alpha_2\delta-1$ domains are indicated. Divalent staple is indicated. SF calcium ions are from $\text{Ca}_v1.2(\Delta C)/\text{Ca}_v\beta_3/\text{Ca}_v\alpha_2\delta-1$ and mark the location of the pore in the $\text{Ca}_v\alpha_2\delta$ -assembled channel. **c**, Superposition of VSD I (yellow orange), PD II (firebrick), and PD III (lime) from the EMC complex (semi-transparent) and their corresponding parts from

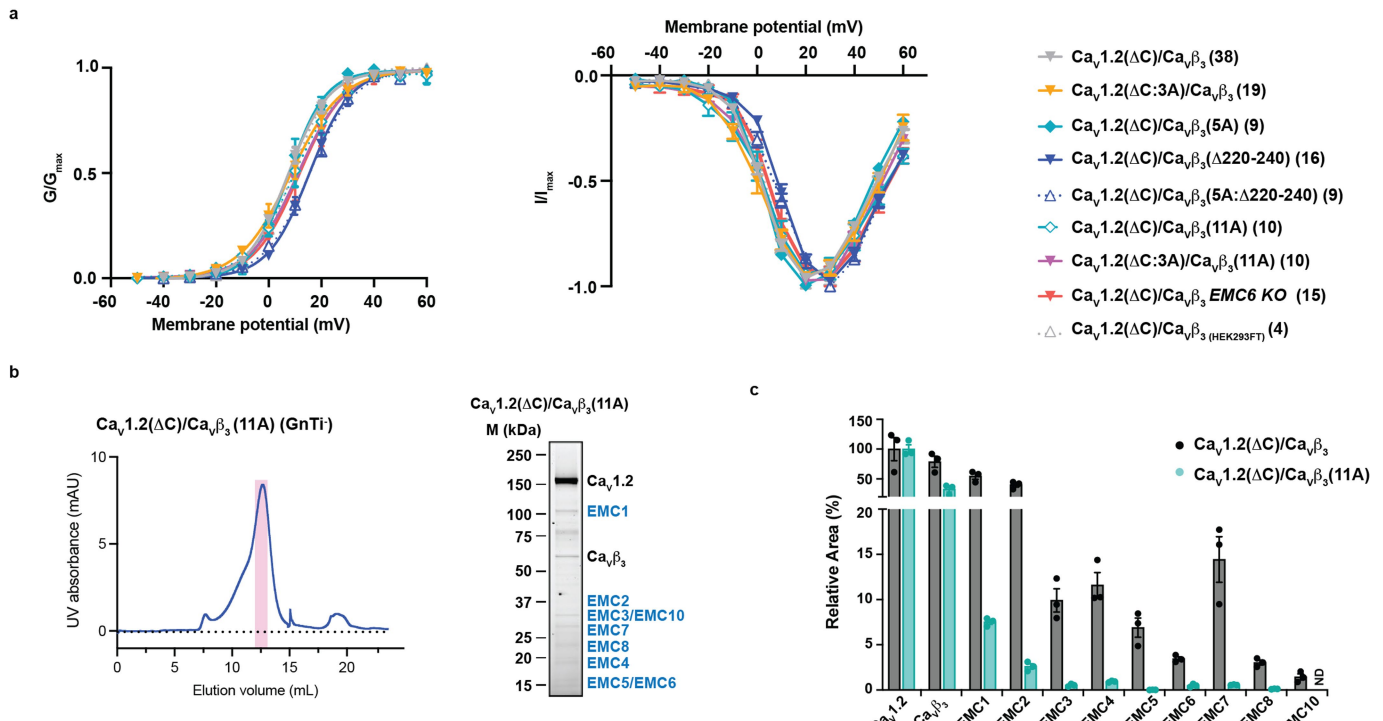
$\text{Ca}_v1.2(\Delta C)/\text{Ca}_v\beta_3/\text{Ca}_v\alpha_2\delta-1$ (slate). $\text{Ca}_v\alpha_2\delta-1$ (aquamarine) is shown as a semi-transparent surface. Calcium ions are from $\text{Ca}_v1.2(\Delta C)/\text{Ca}_v\beta_3/\text{Ca}_v\alpha_2\delta-1$. Left inset shows the coordination of the divalent staple by the VWA domain MIDAS and D151 in $\text{Ca}_v1.2(\Delta C)/\text{Ca}_v\beta_3/\text{Ca}_v\alpha_2\delta-1$. Red distance shows the position of $\text{Ca}_v1.2$ D151 in the EMC complex relative to the calcium ion in the $\text{Ca}_v\alpha_2\delta$ complex. Asterisks mark positions where coordinated alanine mutation impair the ability of $\text{Ca}_v\alpha_2\delta$ to enhance Ca_v currents and surface expression⁵⁹. Right inset shows the extensive contacts between PD II and PD III loops with $\text{Ca}_v\alpha_2\delta$ in the $\text{Ca}_v1.2(\Delta C)/\text{Ca}_v\beta_3/\text{Ca}_v\alpha_2\delta-1$ complex. The PD III loops are disordered in the EMC: $\text{Ca}_v1.2/\text{Ca}_v\beta_3$ complex. $\text{Ca}_v\alpha_2\delta-1$ residues are in italics. **d**, Schematic showing of the conformational changes and interaction sites in the exchange between the EMC: $\text{Ca}_v/\text{Ca}_v\beta$ holdase complex and assembled $\text{Ca}_v/\text{Ca}_v\beta/\text{Ca}_v\alpha_2\delta$ channel. Black ovals indicate key interaction sites in each complex.



Extended Data Fig. 8 | Exemplar purification of Ca_v subunit combinations.

a-c Superose 6 Increase 10/300 GL chromatogram and peak fraction SDS-PAGE for: **a**, Ca_v1.2(ΔC)/Ca_vβ₃ and **b**, Ca_v1.2(ΔC). **c**, Relative detection by mass spectrometry from 'a' and 'b' of EMC proteins with respect to Ca_v1.2(ΔC) across 3 replicates. **d**, Superose 6 Increase 10/300 GL chromatogram and peak fraction SDS-PAGE for Ca_vβ₃. Ca_vβ₃-NK and Ca_vβ₃-SH3 are Ca_vβ₃ proteolytic fragments. ND denotes not detected.

e, Absolute detection of EMC proteins and Ca_vβ₃ by mass spectrometry following expression and purification of Ca_vβ₃. **f**, Superose 6 Increase 10/300 GL chromatogram and peak fraction SDS-PAGE for Ca_v1.2/Ca_vβ₃. Magenta bars in 'a', 'b', 'd', and 'f' mark peak fraction. **g**, Absolute detection of Ca_v1.2, Ca_v1.2(ΔC), Ca_vβ₃, and EMC proteins from 'a' and 'f'. Error bars are calculated as SEM.



Extended Data Fig. 9 | Functional and biochemical characterization of Ca_v mutants. **a**, Voltage dependent activation (left) and I-V relationships (right) for the indicated channels. Parentheses indicate 'n' independent cells examined over >2 independent experiments. **b**, Superose 6 Increase 10/300 GL chromatogram and peak fraction SDS-PAGE for $\text{Ca}_v 1.2(\Delta C)/\text{Ca}_v \beta_3$ (11A). Magenta

bar marks peak fraction. **c**, Relative detection by mass spectrometry from 'b' of EMC proteins with respect to $\text{Ca}_v 1.2(\Delta C)$ across 3 replicates. Data for $\text{Ca}_v 1.2(\Delta C)/\text{Ca}_v \beta_3$ are from Extended Data Fig. 8c. 'ND' indicates 'not detected'. Data in 'a' and 'c' are presented as mean \pm SEM.

Extended Data Table 1 | Statistics for data collection, refinement, and validation

	Cav1.2(ΔC)/Cavβ ₃	Cav1.2(ΔC)/Cavβ ₃ /Cavα _{2δ-1}
Data collection and processing		
Magnification	105,000	105,000
Voltage (kV)	300	300
Electron dose (e-/Å ²)	46	46
Defocus range (μm)	-0.9~1.7	-0.9~1.7
Pixel size (Å)	0.8466	0.8466
Symmetry	C1	C1
Initial particle images (no.)	3,096,005	4,522,745
Final particle images (no.)	217,117	269,950
Map resolution (Å)	3.4	3.6
FSC threshold	0.143	0.143
Map resolution range (Å)	3.0~8.0	3.0~8.0
Refinement	ECAB Map 3 (PDB:8EOI;EMD-28376)	CABAD Map 2 (PDB:8EOG;EMD-28375)
Initial model used (PDB code)	6WW7, 7MIY	7MIY
Model resolution (Å)	3.4	3.5
FSC threshold	0.5	0.5
Map sharpening <i>B</i> factor (Å ²)	-27.6	-82.1
Model composition		
Non-hydrogen atoms	28,721	19,729
Protein residues	3,562	2,416
Ligands	8	22
<i>B</i> factors (Å ²)		
Protein	176.18	129.67
Ligand	105.71	103.42
R.m.s deviations		
Bond lengths (Å)	0.002	0.003
Bond angles (°)	0.494	0.570
Validation		
MolProbity score	2.14	2.06
Clashscore	8.09	11.79
Poor rotamers (%)	2.73	0.51
Ramachandran plot		
Favored (%)	94.6	92.36
Allowed (%)	5.4	7.5
Disallowed (%)	0.03	0.13

Corresponding author(s): MINOR, Daniel, L. Jr.

Last updated by author(s): 19 apr 23

Reporting Summary

Nature Portfolio wishes to improve the reproducibility of the work that we publish. This form provides structure for consistency and transparency in reporting. For further information on Nature Portfolio policies, see our [Editorial Policies](#) and the [Editorial Policy Checklist](#).

Statistics

For all statistical analyses, confirm that the following items are present in the figure legend, table legend, main text, or Methods section.

n/a Confirmed

- The exact sample size (n) for each experimental group/condition, given as a discrete number and unit of measurement
- A statement on whether measurements were taken from distinct samples or whether the same sample was measured repeatedly
- The statistical test(s) used AND whether they are one- or two-sided
Only common tests should be described solely by name; describe more complex techniques in the Methods section.
- A description of all covariates tested
- A description of any assumptions or corrections, such as tests of normality and adjustment for multiple comparisons
- A full description of the statistical parameters including central tendency (e.g. means) or other basic estimates (e.g. regression coefficient) AND variation (e.g. standard deviation) or associated estimates of uncertainty (e.g. confidence intervals)
- For null hypothesis testing, the test statistic (e.g. F , t , r) with confidence intervals, effect sizes, degrees of freedom and P value noted
Give P values as exact values whenever suitable.
- For Bayesian analysis, information on the choice of priors and Markov chain Monte Carlo settings
- For hierarchical and complex designs, identification of the appropriate level for tests and full reporting of outcomes
- Estimates of effect sizes (e.g. Cohen's d , Pearson's r), indicating how they were calculated

Our web collection on [statistics for biologists](#) contains articles on many of the points above.

Software and code

Policy information about [availability of computer code](#)

Data collection

UCSF and Stanford-SLAC Cryo-EM Center (S2C2)
SerialEM v.4.1, Mastronarde, D. N. Automated electron microscope tomography using robust prediction of specimen movements. *J Struct Biol* 152, 36–51, doi:10.1016/j.jsb.2005.07.007 (2005).

Data analysis

cryoSPARC-3.2, Punjani, A., Rubinstein, J. L., Fleet, D. J. & Brubaker, M. A. cryoSPARC: algorithms for rapid unsupervised cryo-EM structure determination. *Nat Methods* 14, 290–296, doi:10.1038/nmeth.4169 (2017).

RELION-3.1 Zivanov, J. et al. New tools for automated high-resolution cryo-EM structure determination in RELION-3. *eLife* 7, doi:10.7554/eLife.42166 (2018).

Phyre2 server, Kelley, L. A., Mezulis, S., Yates, C. M., Wass, M. N. & Sternberg, M. J. The Phyre2 web portal for protein modeling, prediction and analysis. *Nat Protoc* 10, 845–858, doi:10.1038/nprot.2015.053 (2015).

PHENIX, Liebschner, D. et al. Macromolecular structure determination using X-rays, neutrons and electrons: recent developments in Phenix. *Acta Crystallogr D Struct Biol* 75, 861–877, doi:10.1107/S2059798319011471 (2019).

COOT, Emsley, P., Lohkamp, B., Scott, W. G. & Cowtan, K. Features and development of Coot. *Acta Crystallogr D Biol Crystallogr* 66, 486–501, doi:10.1107/S0907444910007493 (2010).

ChimeraX, Pettersen, E. F. et al. UCSF ChimeraX: Structure visualization for researchers, educators, and developers. *Protein Sci* 30, 70–82, doi:10.1002/pro.3943 (2021).

MolProbity, Williams, C. J. et al. MolProbity: More and better reference data for improved all-atom structure validation. *Protein Sci* 27, 293–315, doi:10.1002/pro.3330 (2018).

Electrophysiology data were acquired using Clampex 11.2 (Molecular Devices) and analyzed with Clampfit 10.6 (Molecular Devices).

For manuscripts utilizing custom algorithms or software that are central to the research but not yet described in published literature, software must be made available to editors and reviewers. We strongly encourage code deposition in a community repository (e.g. GitHub). See the Nature Portfolio [guidelines for submitting code & software](#) for further information.

Data

Policy information about [availability of data](#)

All manuscripts must include a [data availability statement](#). This statement should provide the following information, where applicable:

- Accession codes, unique identifiers, or web links for publicly available datasets
- A description of any restrictions on data availability
- For clinical datasets or third party data, please ensure that the statement adheres to our [policy](#)

Coordinates and maps of the EMC:CaV1.2(ΔC)/CaVbeta3 complex (PDB:8EOI; EMD-28376, EMD 28578, EMD-28579, EMD-40559, EMD-40560)) and CaV1.2(ΔC)/CaVbeta3/CaValpha2delta-1 complex (PDB: 8EOG; EMD-28375, EMD-28561, EMD-28564, EMD-40561) are deposited with the RCSB.

Mass spectrometry data is deposited in the Mass Spectrometry Interactive Virtual Environment, (massive.ucsd.edu) under identifier MSV000091736.

Human research participants

Policy information about [studies involving human research participants and Sex and Gender in Research](#).

Reporting on sex and gender

N/A

Population characteristics

N/A

Recruitment

N/A

Ethics oversight

N/A

Note that full information on the approval of the study protocol must also be provided in the manuscript.

Field-specific reporting

Please select the one below that is the best fit for your research. If you are not sure, read the appropriate sections before making your selection.

Life sciences

Behavioural & social sciences

Ecological, evolutionary & environmental sciences

For a reference copy of the document with all sections, see nature.com/documents/nr-reporting-summary-flat.pdf

Life sciences study design

All studies must disclose on these points even when the disclosure is negative.

Sample size

Selected as appropriate for the experiment (i.e. CryoEM, N=2-3, electrophysiology N=>4)

Data exclusions

No data were excluded from the analyses

Replication

For two electrode voltage-clamp studies, the results are from at least two independent oocyte batches. n = 7-8 oocytes ('n' value is shown at the end of Figure S2 legend).

For whole cell patch clamp studies, the results are from at least three independent tranformations. n=4-31 cells ('n' value is shown in Fig. 5c).

For mass spectrometry analysis, experiments were performed in experimental triplicate. Specifically, samples were analyzed 3 separate times via SDS-PAGE separate followed by in-gel digestion and mass spectrometry analysis protocols as described. All attempts at replication were successful.

Randomization

N/A

Blinding

N/A

Reporting for specific materials, systems and methods

We require information from authors about some types of materials, experimental systems and methods used in many studies. Here, indicate whether each material, system or method listed is relevant to your study. If you are not sure if a list item applies to your research, read the appropriate section before selecting a response.

Materials & experimental systems

n/a	Involved in the study
<input type="checkbox"/>	<input checked="" type="checkbox"/> Antibodies
<input type="checkbox"/>	<input checked="" type="checkbox"/> Eukaryotic cell lines
<input checked="" type="checkbox"/>	<input type="checkbox"/> Palaeontology and archaeology
<input type="checkbox"/>	<input checked="" type="checkbox"/> Animals and other organisms
<input checked="" type="checkbox"/>	<input type="checkbox"/> Clinical data
<input checked="" type="checkbox"/>	<input type="checkbox"/> Dual use research of concern

Methods

n/a	Involved in the study
<input checked="" type="checkbox"/>	<input type="checkbox"/> ChIP-seq
<input checked="" type="checkbox"/>	<input type="checkbox"/> Flow cytometry
<input checked="" type="checkbox"/>	<input type="checkbox"/> MRI-based neuroimaging

Antibodies

Antibodies used

Anti-GFP nanobody

Validation

Made and validated as described in Ref. 76

Eukaryotic cell lines

Policy information about [cell lines and Sex and Gender in Research](#)

Cell line source(s)

HEK293S GnTI- (ATCC) , HEK293FT, HEK293FT-EMC5 KO, HEK293FT-EMC6 KO Vorhees lab, CalTech (HEK293FT, HKE293FG-EMC5 KO, HEK293FT- EMC6 KO)

Authentication

ATCC (HEK293SGnTI-), Vorhees lab, CalTech (HEK293FT, HKE293FG-EMC5 KO, HEK293FT- EMC6 KO)

Mycoplasma contamination

negative

Commonly misidentified lines
(See [ICLAC](#) register)

n/a

Animals and other research organisms

Policy information about [studies involving animals; ARRIVE guidelines](#) recommended for reporting animal research, and [Sex and Gender in Research](#)

Laboratory animals

Xenopus laevis

Wild animals

No wild animals were used in this study.

Reporting on sex

Oocytes were collected from female frogs.

Field-collected samples

No field collected samples were used.

Ethics oversight

Oocytes were harvested from female Xenopus laevis frogs (Nasco Cat# LM00531) and housed in the UCSF Laboratory Animal Resource Center (LARC) facilities. The use of these Xenopus oocytes was approved by IACUC (protocol approval # AN193390 - 01B) and experiments were performed in accordance with University of California guidelines and regulations.

Note that full information on the approval of the study protocol must also be provided in the manuscript.